Journal of Wind Engineering & Industrial Aerodynamics 258 (2025) 106009

Contents lists available at ScienceDirect

Journal of Wind Engineering & Industrial Aerodynamics

journal homepage: www.elsevier.com/locate/jweia

Investigating low-frequency turbulence effects on building roof pressures through active flow control in a large boundary layer wind tunnel

Nasreldin O. Mokhtar [a], Pedro L. Fernández-Cabán [a,*], Ryan A. Catarelli [b]

[a] Florida A&M University–Florida State University (FAMU-FSU) College of Engineering, Tallahassee, FL, USA
[b] University of Florida, Gainesville, FL, USA

ARTICLE INFO

Keywords:
Integral length scales
Wind pressure coefficients
Large-scale turbulence
Active turbulence simulation
Peak pressures
Boundary layer wind tunnel
TTU WERFL building

ABSTRACT

This study examines the effect of incident large-scale (low-frequency) turbulence on the wind pressure field acting on low-rise building roofs. Large-scale turbulence modulation was enabled by a high-performance 3 m × 6 m multi-fan array, termed Flow Field Modulator (FFM), situated at the upwind section of a large boundary layer wind tunnel (BLWT). The FFM was leveraged to actively generate low-frequency wind velocity fluctuations in the BLWT and operated in conjunction with a mechanized roughness element grid to simulate large- and small-scale turbulent atmospheric boundary layer flows. Aerodynamic pressure measurements were monitored on the surface of a 1:20 scale low-rise building model under multiple turbulent length scales and intensities. Experimental results demonstrate how, for similar turbulence intensity levels, higher correlation of pressure fluctuations in flow detachment zones are observed with increasing turbulent scales. Larger integral length scales were also linked to more pronounced non-Gaussian behavior (i.e., higher skewness) of local pressure signals in flow separation zones and along the path of conical vortices developed above the roof of the building model in the case of cornering wind azimuths. Finally, the study highlights how stronger non-Gaussian trends and increased pressure correlations lead to higher local and area-average peak suction roof loads.

1. Introduction

Atmospheric boundary layer (ABL) wind flows transport a broad range of turbulent scales that interact with the built environment. In the case of bluff body structures (e.g., buildings), the size and duration of such turbulent eddies can influence the magnitude and spatial distribution of aerodynamic wind loads imposed on the building's envelope. Specifically, the intensity of extreme negative (suction) loads developed near flow-separated regions (e.g., roof edges/corners) of sharp-edge bluff bodies have been directly linked to the freestream turbulent characteristics of the incident wind field (e.g. Gartshore, 1973, 1984; Bearman and Morel, 1983; Saathoff and Melbourne, 1997).

Knowledge regarding the effects of freestream turbulence on bluff body aerodynamics has been derived almost exclusively from experiments in atmospheric boundary layer wind tunnels (ABLWT). The bulk of these ABLWT studies were conducted using relatively small building models (<1:50) with geometric (length) scales proportional to the depth of the simulated ABL wind field. While larger building models may be desirable to alleviate existing drawbacks associated with reduced-scale ABLWT testing including: (1) the limited spatial pressure resolution of instrumented models; (2) the mismatch in Reynolds number, and (3) the difficulty of integrating minor architectural features in models with complex geometries) (Mooneghi et al., 2016; Gan Chowdhury et al., 2017), precise control of large-scale (low frequency) turbulence in conventional ABLWT flows has proven challenging.

Traditional ABLWT facilities are often equipped with passive (static) turbulence-generating devices (e.g., vortex generators, roughness grids, castellated barriers, etc.), which are strategically placed along the longitudinal tunnel dimension to achieve desired (target) ABL flow conditions. Particularly, incident turbulence levels at ABLWT testing sections are primarily calibrated by adjusting the morphometric properties (e.g., height and horizontal arrangement) of roughness element arrays situated upwind to the model. However, the generation of large-scale (low frequency) turbulent fluctuations via passive flow conditioning strategies becomes increasingly difficult as simulation scales increase. For example, large-scale wind tunnel facilities often exhibit deficiencies in the production of large-scale turbulence (LST) with increasing scales (>1:50) (Jayakumari et al., 2023), which prevents researchers and engineers from calibrating ABLWT flows to target ABL turbulence spectra models (Von Kármán, 1948). Such deficiencies in LST have led to the development of partial turbulence simulation (PTS) approaches, where

* Corresponding author.
E-mail addresses: nasreldin1.mokhtar@famu.edu (N.O. Mokhtar), plfernandez@eng.famu.fsu.edu (P.L. Fernández-Cabán), rcatarelli@ufl.edu (R.A. Catarelli).

https://doi.org/10.1016/j.jweia.2025.106009
Received 14 June 2024; Received in revised form 27 November 2024; Accepted 6 January 2025
Available online 29 January 2025

Nomenclature

ABL	Atmospheric boundary layer
ABLWT	Atmospheric boundary layer wind tunnel
BLWT	Boundary layer wind tunnel
DFT	Discrete Fourier transforms
EF	Experimental facility
FFM	Flow Field Modulator
GCA	Governing Convergence Algorithm
LST	Large-scale turbulence
NHERI	Natural Hazards Engineering Research Infrastructure
PTS	Partial turbulence simulation
QS	Quasi-steady
SSL	Separated shear layer
TTU	Texas Tech University
TL	Tap line (or line transect)
UF	University of Florida
WERFL	Wind Engineering Research Field Laboratory
A	Roof panel area
a_j	Tributary area of pressure tap j
C_p	Pressure coefficient
$\overline{C}_p$	Mean pressure coefficient
C'_p	Standard deviation pressure coefficient
$\widehat{C}_p$	Peak pressure coefficient
$\widehat{C}_{p,AVG}$	Area-average peak pressure coefficient
$C_{p,AVG}(t)$	Area-average pressure time history
$\mathrm{cov}(p_1, p_2)$	Covariance between two local (tap) pressure signals
f	Frequency
f_c	Cut-off frequency
f_m	Frequency at Melbourne parameter ($10\overline{u}/H$)
H	Eave height of low-rise building
i	Rank order of local peak pressures
I_u	Longitudinal turbulence intensity
$I_{u,T}$	Target longitudinal turbulence intensity
L_u^x	Longitudinal integral length scale
M	Mode parameter of extreme value fit
$1/\alpha$	Dispersion parameter of extreme value fit
N	Number of sample peaks
n_t	Number of pressure taps
p	Local (tap) air pressure
p_∞	Ambient static air pressure
p'_{static}	Reference static air pressure fluctuations
p'_{tot}	Reference total air pressure fluctuations
p'_{dyn}	Reference dynamic air pressure fluctuations
$\overline{u}$	Longitudinal mean velocity
$\overline{u}_H$	Longitudinal mean velocity at eave height
ρ	Air density
ρ_{uu}	Autocorrelation of longitudinal velocity component
Re	Reynolds number ($=\overline{u}H/\nu$)
R_{pp}	Pearson's correlation coefficient between local (tap) pressure signals
x, y, z	Longitudinal, lateral, and vertical wind tunnel coordinates
τ	Time lag (delay)
S_{uu}	Power spectral density of longitudinal velocity fluctuations
S	Melbourne (small-scale) parameter
y_R	Reduced variate
ν	Kinematic viscosity of air
u, v, w	Longitudinal, lateral, and vertical wind velocity components
α, β, γ	Terrain constants
σ_{p1}, σ_{p2}	Standard deviation of two local (tap) pressure signals

only small-scale (high frequency) turbulence is physically simulated in the wind tunnel and LST effects are analytically modeled using quasi-steady (QS) theory (Mooneghi et al., 2016; Irwin, 2008). However, validation of these QS approaches for wind pressure prediction have been performed using limited full-scale observations and taken under a reduced set of turbulent/terrain conditions (e.g., open exposure).

The linkage between building aerodynamics to large-scale turbulence has been largely assessed on two-dimensional (2D) bodies (e.g. Gartshore, 1973, 1984; Melbourne, 1979; Castro and Haque, 1988; Kiya and Sasaki, 1983; Hillier and Cherry, 1981; Saathoff and Melbourne, 1997). For instance, Saathoff and Melbourne (1997) examined the influence of upstream turbulence characteristics on the flow field around a 2D rectangular prism. Their study explored a broad range of turbulence intensity and length scales with $L_u^x/D = 0.4$ to 2.1, where D was the thickness of a 2D flat plate with a rectangular cross-section ($D = 50$ mm). Their research demonstrated that freestream turbulence induces (1) significant disruptions to the separated shear layer (SSL) resulting in shorter mean reattachment lengths, (2) larger surface pressure fluctuations occurring in closer proximity to the leading edge, and (3) greater surface pressure fluctuations for larger integral length scales. They also observed that the location of maximum surface pressure fluctuations remained unaffected by the integral scales within the investigated range. This was corroborated by the detailed flow measurements in Lander et al. (2016).

Li and Melbourne (1999) explored the flow patterns just after the incident wind flow separates from the edge of a 2D flat blunt surface and noted that as turbulence intensity increases from $I_u = 8\%$ to $I_u = 20\%$, the effect of turbulence scale on peak pressures becomes more significant. At lower intensities, the turbulence scale, which was $L_u^x/D = 6$, has less impact on fluctuating and negative peak pressures than at higher intensities. Also, their study found that larger turbulence scales heighten pressure fluctuations within the separation bubble.

Studies such as those by Gartshore (1973) and more recently by Lander et al. (2016), have focused on the impact of small-scale turbulence on SSL development, observing earlier turbulence onset closer to the leading edge, and that turbulence on the stagnation streamline significantly alters the separated flow. The transition to turbulence in the separated flow is immediate after separation due to a bypass mechanism. Larger length scales of upstream turbulence increase the coherence of shear layer roll-up while decreasing small-scale turbulence perturbation (Saathoff and Melbourne, 1997). These enhanced vortices generated from the leading edge contribute to increased surface pressure fluctuations.

Due to challenges associated with the physical modulation of LST in ABLWT, the bulk of the research concerning incident turbulence effects on 3D building aerodynamics has focused on small-scale turbulence (e.g. Tieleman et al., 1978, 1994, 2003; Hajj et al., 2000; Tieleman, 2003; Akon and Kopp, 2016, 2018; Fernández-Cabán and Masters, 2018; Morrison and Kopp, 2018). Most of these studies relied on modifying turbulent intensity (I_u) levels at the testing section by adjusting roughness grid morphometry upstream to the building model (Hajj et al., 2000). For instance, Tieleman et al. (2003) conducted ABLWT studies on a 1:50 model of the Texas Tech University (TTU) Wind Engineering Research Field Laboratory (WERFL) experimental building to map the dependence of mean, rms, and peak wind pressures on incident turbulence. They investigated a range of I_u between 7.1% and 19.3% (at the prism height $= H$) and integral length scales (L_u^x) were between 2.6 and 8.6 times larger than H. The flow conditions were achieved using a variety of spires and manual adjustment of the upwind surface roughness grid.

More recently, Akon and Kopp (2016) performed pressure tests on a 1:50 TTU model and reported that increased upstream turbulence intensity was found to reduce the sizes of mean separation bubbles on roofs, which also generally heightens fluctuations of wind-induced suctions on roofs. Further, this change in separation bubble size directly impacts the distribution of mean roof surface pressures. The fluctuating component of roof surface pressures is also dependent on upstream turbulence (Tieleman, 2003; Akon and Kopp, 2016). This observation was independently validated in Fernández-Cabán and Masters, (2018).

Akon and Kopp, (2018) leveraged Particle Image Velocimetry (PIV) to investigate the physics underlying separated-reattaching flows over the roof surface of a 3D low-building model under six different turbulent boundary layer conditions. They found that while the mean flow field above the roof surface displayed similar behavior for the six terrain conditions, distinct differences were observed in turbulent stresses, which they attributed to high levels of initial turbulence kinetic energy in the separated shear layer. While the study examined a wide range of turbulence intensities (between 14% and 26% at the roof height; H), the range of L_u^x/H was limited.

Full-scale experiments performed by Morrison and Kopp (2018) at the IBHS Research Center investigated the effects of turbulence intensity and scale on surface pressure fluctuations on the roof of a full-scale replica of the TTU building. The study revealed that incident turbulence in the streamwise direction with frequencies in the range $0.1 < fH/\overline{u} < 2$ govern the intensity and distribution of surface pressure fluctuations near the roof edge in the ABL. However, physical generation of low-frequency turbulent scales below frequencies of $fH/\overline{u} < 0.1$ proved challenging.

To address this experimental limitation, studies in recent decades have explored solutions to account for the missing low-frequency turbulence through analytical approaches based on QS models (e.g. Banks and Meroney, 2001; Guo et al., 2021; Richards and Hoxey, 2004, 2008, 2012; Richards et al., 2007; Wu and Kopp, 2016, 2018, 2019; Stenabaugh et al., 2015; Mooneghi et al., 2016; Irwin, 2008). For instance, Banks and Meroney (2001) used simultaneous pressure and velocity BLWT data to assess the basic assumption of QS theory (i.e., building surface pressure fluctuations are directly related to fluctuations in the local wind vector). This assumption is found to be mainly valid for cornering mean wind azimuths ($\overline{\theta}$) and low-frequency changes in $\overline{\theta}$. The work also documented that QS theory ignores the random vortex motions (e.g., body generated turbulence) and how they contribute to pressure fluctuations in flow separation zones.

Richards and Hoxey (2004) developed a QS method for predicting peak pressures from observed mean pressure coefficients. Their approach calculated the joint probability of instantaneous wind azimuths and gust dynamic pressure for wall pressure estimates. In the case of roof pressures, elevation angle of the incident wind field was also incorporated in the QS. The study showed reasonable agreement with field data derived from a full-scale 6-m cube (Silsoe building). Richards and Hoxey (2012) continued their exploration of quasi-steady and other processes (building-generated turbulence) affecting pressures on the 6-m Silsoe building, providing a more refined understanding of the dynamics of surface pressure and the limitations of various modeling approaches. An enhanced version of these QS models have been more recently developed by Wu and Kopp (2016). For example, Wu and Kopp, 2018, 2019 conducted studies focusing on the effects of upstream (primarily small-scale) turbulence characteristics on pressure fluctuations on a low-rise building and the physical assumptions of a quasi-steady vector model.

Irwin, 2008 suggested differentiating between small- and large-scale turbulence effects on wind loading. Following this, Mooneghi et al. (2016) introduced the partial turbulence simulation (PTS) method, where small-scale turbulence is physically simulated in the wind tunnel, and QS theory is analytically applied to the physical pressure data to account for the absence of low-frequency turbulence. Recently, Guo et al., (2021) developed a new method to estimate peak pressures on low-rise building models based on QS theory and PTS analysis through Monte Carlo simulation base on independent assumption of small- and large-scale turbulence, enhancing the prediction of peak area-averaged pressure coefficients.

While small-scale turbulence can be readily simulated using passive roughness grids, some researchers have moved to active flow conditioning strategies to impart large-scale turbulence (LST) into wind tunnel flows (Bienkiewicz et al., 1983; Kobayashi and Hatanaka, 1992; Nishi et al., 1993; Nishi and Miyagi, 1995; Nishi et al., 1997; Nishi et al., 1999; Shuyang et al., 2001; Cao et al., 2002; Ozono et al., 2006; Ozono and Ikeda, 2018; Mokhtar et al., 2024; Mokhtar et al., 2023). Previous attempts involved 2D active grid systems, with Bienkiewicz et al. (1983) successfully introducing larger gust structures through vertical in-plane grid oscillations. Kobayashi and Hatanaka (1992) explored experimental approaches to actively control streamwise and vertical flow velocity components using dynamic actuation of 2D arrays of plates and airfoils. Nishi et al. (Nishi et al., 1993; Nishi and Miyagi, 1995) pioneered computer-controlled multi-fan array systems for simulating large-scale ABL turbulence using iterative correcting approaches based on sensor feedback from velocity probe readings.

Subsequent works developed active simulation capabilities that included user-specified targets to achieve desired flow conditions at the wind tunnel test section (Nishi et al., 1997, 1999; Shuyang et al., 2001; Cao et al., 2002). Ozono et al., (2006) devised a multi-fan wind tunnel (MFWT) that generated homogeneous turbulence within a short downstream distance. In their study, they achieved turbulence intensities ranging between 12% and 16%, and integral length scales between 0.6 and 0.7 m. More recently, Mokhtar et al. (2024) used an active 3 m × 6 m (2D) multi-fan array, termed Flow Field Modulator (FFM), in a large BLWT at the University of Florida (UF) Natural Hazards Engineering Research Infrastructure (NHERI) Experimental Facility (EF) (Catarelli et al., 2020b) to achieve prescribed ABL turbulent lengths scales of approximately one order of magnitude larger than the ones obtained through passive flow conditioning strategies. Their work examined a wide range of turbulence intensity levels (from 15% to 30%) and demonstrated the FFM's capability to achieve integral length scales of up to $L_u^x/H \sim 40$ for 1:20 BLWT simulations (where $H = 19.8$ cm). The present work aims at leveraging the active turbulence modulation to map the intensity and distribution of 3D aerodynamic loading action on low-rise buildings under highly turbulent flows with length scales significantly larger than the characteristic building dimension (e.g, H).

This study seeks to systematically assess the effect of LST on aerodynamic building loads through active low-frequency turbulence generation. The research leveraged a high-performance 3 m × 6 m (2D) fan array to achieve ABL turbulent scales significantly greater than previously achieved in BLWTs of similar cross-sections. Multiple incident turbulent intensities (I_u) and integral length scales (L_u^x) were examined to characterize the impact of small- and large-scale turbulence on mean, fluctuating, and peak pressures on the roof of a low-rise structure. The paper first (Section 2) describes the active and passive flow conditioning systems used for a series aerodynamic BLWT tests conducted at the UF NHERI EF (Catarelli et al., 2020b). Results highlighting the influence of large-scale turbulence on aerodynamic loading are presented in Section 3. This is followed by Section 4, which discusses the limitations of the BLWT experiments and subsequent research directions. Finally, Section 5 summarizes key research findings and potential implications regarding wind load provisions.

2. Experimental setup

Aerodynamic tests were conducted at the UF BLWT (Catarelli et al., 2020b), a low-speed open-circuit tunnel with dimensions of 6 m (W) × 3 m (H) × 38 m (L). The primary UF BLWT flow conditioning components include the (1) vaneaxial fan bank, (2) the Flow Field Modulator (FFM),

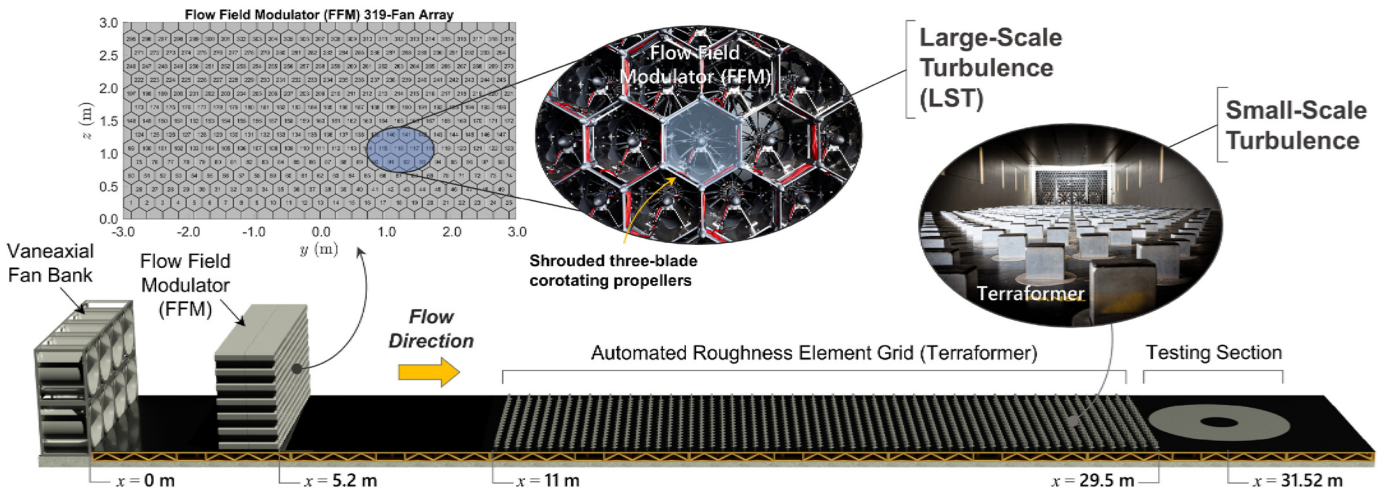

Fig. 1. Layout of active and passive flow conditioning systems at the UF BLWT.

and (3) the Terraformer roughness grid (Fig. 1). The vaneaxial fan bank has a 2 × 4 (vertical × lateral) 448 kW fan array, and the system is responsible for driving the mean mass flow along the BLWT. The FFM and Terraformer systems were used in this study to control large- and small-scale turbulence at the downwind test section, respectively. Sections 3.1. and 3.2 detail how these two flow conditioning systems operate.

Injection of large-scale turbulent flow fluctuations was achieved via the FFM, a high-resolution flow control device located in the upwind section of the UF BLWT. The FFM is a computer-controlled 240 kW 3 m (H) × 6 m (W) 2D fan array comprising 319 hexagonal aluminum cells. Each FFM cell has shrouded three-blade corotating propeller pairs with high-performance 750-W brushless DC motors driven by electronic speed controllers (ESC). Command signals are sent to each ESC by two NI cRIO-9048 eight-slot chassis with NI-9403 C Series digital communication modules controlled by a custom FFM virtual instrument (VI). This hardware configuration enables a maximum free discharge velocity of +20/-17 m/s. The FFM 319 fan bank resides immediately upwind to a dimensionally identical 319-cell honeycomb system.

This study integrated a computer-controlled roughness element array, called the Terraformer (Fig. 1), to mechanically generate and adjust small-scale turbulent content at the BLWT test section. The Terraformer is an 18 m long (fetch length) 18 × 62 roughness element grid system. The system is fully mechanized and consists of 1116 integrated stepper motor assemblies that precisely rotate and translate roughness elements independently from one another to control height and orientation. Each roughness element has plan dimensions of 5 cm by 10 cm, and the heights can vary from 0 cm (element flush with tunnel floor) to 16 cm. Additional information regarding the Terraformer system can be found in Catarelli et al., 2020a, 2020b.

The wind tunnel building specimen was constructed and instrumented at the UF NHERI EF and consisted of a rigid 1:20 scaled representation of the Texas Tech University (TTU) Wind Engineering Research Field Laboratory (WERFL) experimental building (Levitan and Mehta, 1992a, 1992b). The model's flat faces (walls and roof) were fabricated from 0.22" (5.6 mm) thick clear plastic (polycarbonate) sheets, and the roof perimeter consisted of interchangeable 3D printed parts, which enabled future testing of other architectural/geometric features (e.g., parapet, spoilers, rounded edge) (Mokhtar et al., 2025). However, in this study, the 1:20 building model was only tested using the actual roof geometry of the TTU WERFL building (i.e., 1:48 sloped gable roof with sharp edges along the roof's perimeter). A representative BLWT configuration is depicted in Fig. 2a. Incident mean and turbulent profile measurements were monitored during aerodynamic testing using 12 five-hole Vectoflow velocity probes mounted to an automated instrument traverse system. The probes were set to measurement heights z = 5, 10, 15, 19.8, 25, 30, 52.5, 72.5, 95, 115, 137.5, and 157.5 cm above the BLWT floor and horizontally positioned at the BLWT location x = 31 m and y = 1.35 m (position B in Fig. 2b).

The building model was instrumented with 376 pressure sensors (taps) on the roof and 56 taps on the four walls (432 total taps), as shown in Fig. 3. The horizontal coordinates of roof taps were symmetric (i.e.,

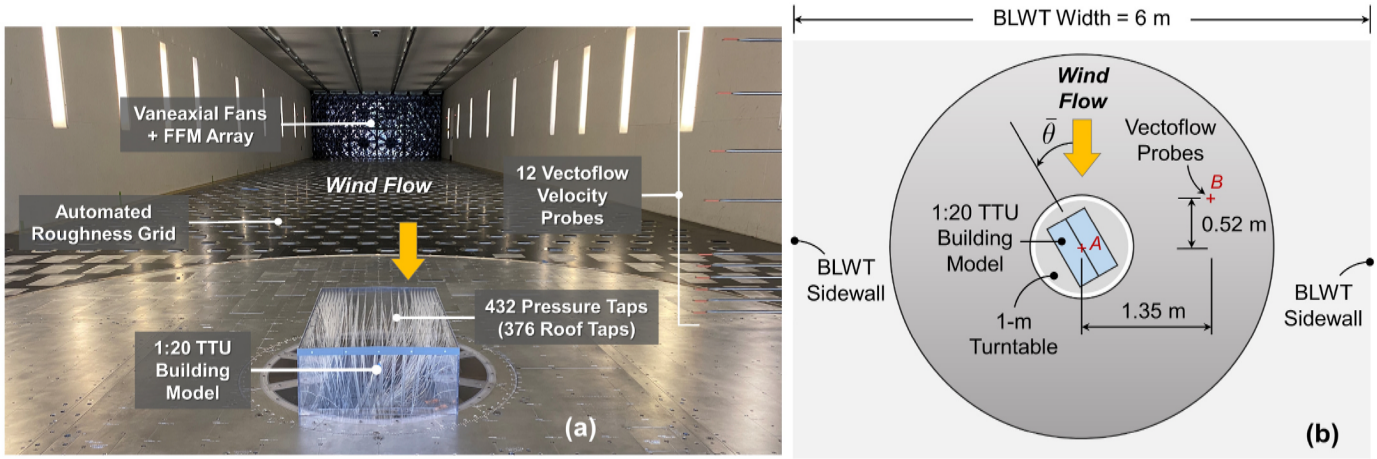

Fig. 2. Experimental setup for aerodynamic tests performed on the 1:20 TTU model.

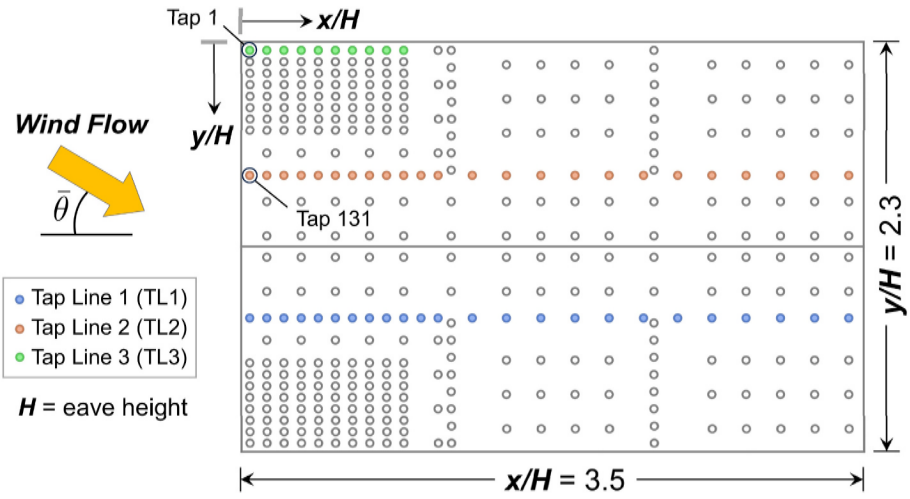

Fig. 3. Roof dimensions and pressure tap layout of the 1:20 TTU building model.

mirrored) about the long building dimension to provide redundancy in pressure data at wind azimuths of $\bar{\theta} = 0°$. All 432 pressure taps were connected to a 512-channel Scanivalve system via 48″ long urethane tubes with an outer diameter (O.D.) of 0.063" (1.59 mm). Pressure coefficients were computed as follows:

$$C_p = \frac{p - p_\infty}{0.5\rho\bar{u}_H{}^2} \tag{1}$$

where $p - p_\infty$ is the local (tap) gauge pressure; ρ is the air density; and $\bar{u}_H$ is the reference mean flow velocity taken by the Vectoflow sensor position at the eave height of the building model ($H = 0.198$ m). The sampling rate for the Vectoflow and Scanivalve measurements were 850 Hz and 625 Hz, respectively.

Two post-processing filters were applied to the local (tap) pressure measurements. First, dynamic tubing response corrections described in Fernández-Cabán and Masters (2020) were applied using frequency response (transfer) functions developed for the specific tube and (inner) diameter sizes used to instrument the building model. Fig. 4 illustrates the transfer function for the 48" tubing system used. Second, active generation of low frequency (less than ~6 Hz) velocity fluctuations in the BLWT produced non-negligible static pressure fluctuation (p'_{static}) at the BLWT testing section. During aerodynamic testing, these static pressure fluctuations were monitored by the Vectoflow sensor at Position B and a height $z = 0.198$ (i.e., roof height) and digitally filtered from local (tap) pressure signals. Filtering was performed in the frequency domain, where Discrete Fourier transforms (DFT) were applied to mean-removed total (p'_{tot}) and dynamic (velocity) pressure (p'_{dyn})

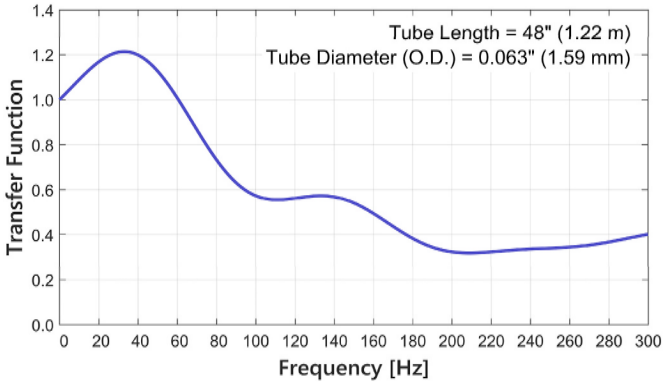

Fig. 4. Transfer function of the tubing system applied to correct local (tap) pressure signals.

signals collected by the Vectoflow probe at $z = 19.8$ cm (where $p'_{tot} = p'_{static} + p'_{dyn}$). The amplitude ratio of p'_{tot} and p'_{dyn} was then used to attenuate low frequency p'_{static} amplitudes from the local (tap) pressure readings in the frequency domain. Lastly, an inverse DFT was applied to convert the corrected tap pressure signal back to the time domain. Fig. 5 depicts a representative example of the filtering process applied to Tap 131 for a wind azimuth of $\bar{\theta} = 0°$ (see Fig. 3).

Input settings for the UF BLWT flow conditioning systems (i.e., vaneaxial fans, FFM, and Terraformer roughness grid) calibrated in Mokhtar et al., 2024 and (Mokhtar et al., 2023) were adopted in this study to recreate a range of actively generated turbulence intensities (I_u) and integral length scales (L_u^x). To achieve target (user-specified) ABL turbulence levels at the BLWT testing section, Mokhtar et al. (2024) implemented a Governing Convergence Algorithm (GCA) (Pinyochotiwong, 2022) to iteratively adjust input settings of the vaneaxial fans, FFM, and Terraformer roughness grid. Adjustments were based on sensor feedback from the 12 Vectoflow velocity probes that monitored the flow conditions at the BLWT testing section. For all experiments, the target longitudinal mean velocity at $H = 0.198$ m was approximately 6 m/s. A detailed description of the GCA and the flow calibration procedures used in this study to achieve the target mean and turbulent wind profiles are presented in Mokhtar et al. (2024).

Table 1 includes measured turbulent conditions captured during BLWT aerodynamic tests (Vectoflow probe locations shown in Fig. 2b). The TTU model was immersed in eight (actively generated) large-scale turbulent (LST) flow conditions. LST ID cases 1–4 comprise moderate turbulence intensity levels (15%), and LST cases 5–8 represent high levels of I_u (30%). While the flow calibration procedures detailed in Mokhtar et al. (2024) were conducted at the center ($x = 31.52$ m, $y = 0$ m; position A in Fig. 2b) of the BLWT test section (i.e., in the absence of the building model), measured I_u and L_u^x values obtained at the new Vectoflow probe location ($x = 31$ m, $y = 1.35$ m; position B in Fig. 2b) agree well with observations from the original flow calibration tests.

3. Results

Fig. 6 highlights the range of achievable small- and large-scale incident turbulent flow conditions in the BLWT largely enabled by the FFM and Terraformer subsystems. Square (blue) data points indicate velocity probe measurements taken under traditional (i.e., baseline) BLWT conditions (Fernández-Cabán and Masters, 2018) where mechanical turbulence was only introduced passively by the Terraformer (no active FFM turbulence modulation). Circular (yellow and green) markers correspond to turbulent flow statistics, from 20 s velocity time

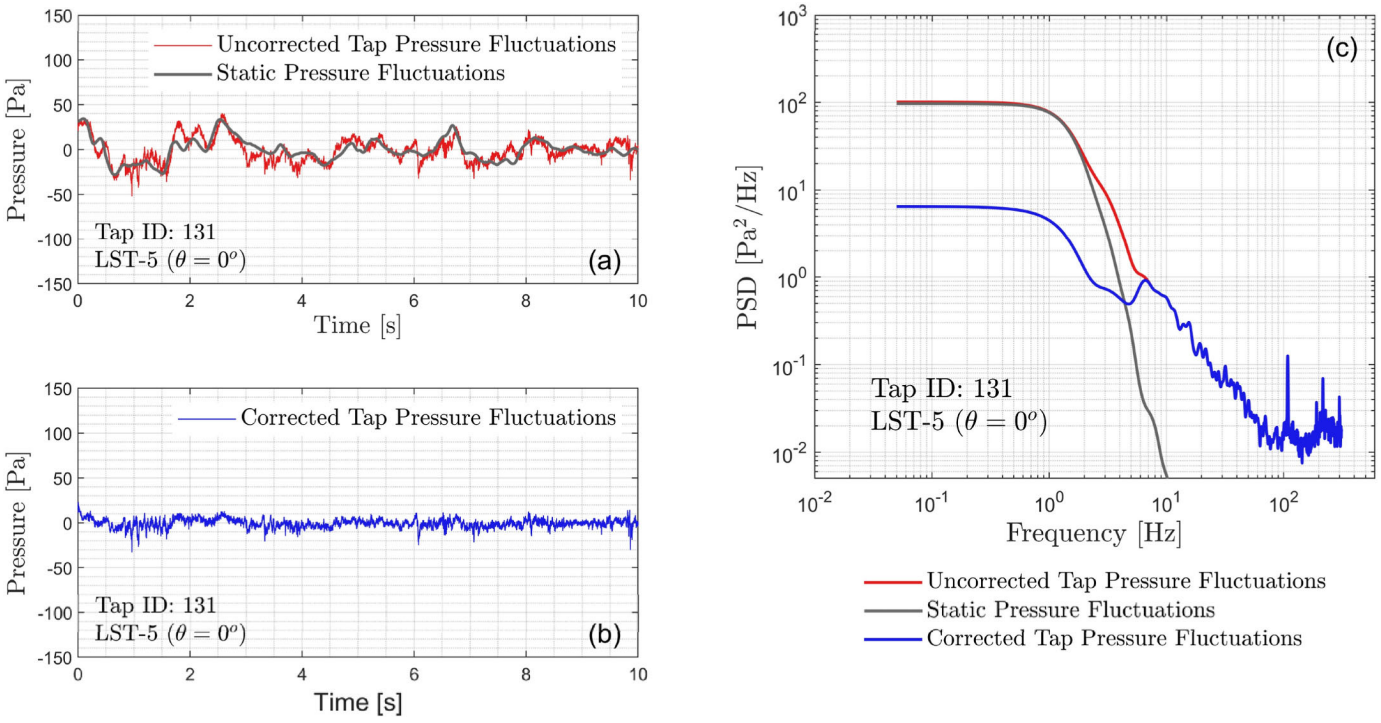

Fig. 5. Local pressure correction (Tap 131) for low-frequency (FFM-generated) static pressure fluctuations in the BLWT.

Table 1
Turbulent flow statistics at the eave height ($z = H = 0.198$ m) of the 1:20 TTU model.

BLWT ID	$I_{u,T}$ (Target)	$L^x_{u,T}/H$ (Target)	Turbulence Intensity, I_u		Length Scale, L^x_u/H		S^6 Eq. (3)	
			$\overline{\theta} = 0°$	$\overline{\theta} = 45°$	$\overline{\theta} = 0°$	$\overline{\theta} = 45°$	$\overline{\theta} = 0°$	$\overline{\theta} = 45°$
LST-1	0.15	5.1	0.14	0.15	7.3	7.9	108	124
LST-2		15	0.14	0.15	9.7	9.8	123	144
LST-3		25	0.16	0.17	26	23	159	196
LST-4		35	0.17	0.18	23	23	299	380
LST-5	0.3	5.1	0.31	0.30	5.7	5.5	764	936
LST-6		15	0.34	0.33	9.4	7.3	689	715
LST-7		25	0.32	0.32	18	21	299	380
LST-8		35	0.32	0.32	30	28	294	433

series, generated by modulating low-frequency turbulence using the FFM subsystem. Integral length scale (L^x_u) estimates were obtained from velocity time histories by applying Taylor's "frozen" turbulence hypothesis, where L^x_u is obtained as follows:

$$L^x_u = \overline{u} \int_0^\infty \rho_{uu}(\tau) d\tau \tag{2}$$

in which ρ_{uu} is the autocorrelation of the longitudinal velocity component; and τ is the time lag. Representative autocorrelation plots of similar FFM-generated flows can be found in Mokhtar et al. (2024).

In Fig. 6b, small-scale turbulence was quantified by measuring the incident turbulence content at a frequency equivalent to 10 times the characteristic dimension of the building (i.e., 10 H; where H is the eave height of the model). The turbulent energy at this frequency is known as the Melbourne parameter S (Melbourne, 1980) and is defined in Tieleman (2003) as:

$$S = \frac{f_m S_{uu}(f_m)}{\overline{u}^2} \times 10^6 \tag{3}$$

where S_{uu} is the one-sided power spectral density (PSD) of turbulent velocity fluctuations; $\overline{u}$ is the mean velocity; and $f_m = 10\overline{u}/H$. The S parameter is loosely associated with the turbulent content of the incident flow with a wavelength comparable to the thickness of the separated shear layer (SSL). Tieleman (2003) details that for a low-rise structure, such SSL thickness is approximately 1/10 of the building height (H). Fig. 6 reveals how traditional (i.e., baseline) BLWT configuration can achieve a broad range of S values (from 0.1 to 1.9×10^3). In the UF BLWT, the larger S values are associated with higher (i.e., rougher) upwind terrain morphometries enabled by the Terraformer (see Fig. 1).

Fig. 6a shows the large range of L^x_u/H achieved across multiple turbulence intensities ($I_u = \sigma_u/\overline{u}$), with maximum length scales exceeding 40 H. It is noticeable from Fig. 6a that FFM (yellow) data points are clustered around three specific turbulence intensity levels, namely $I_u =$ 0.15, 0.2, and 0.3. These correspond to the three (user-specified) target turbulence levels (or $I_{u,T}$) selected when calibrating the BLWT flows (Mokhtar et al., 2024). In this study, only $I_{u,T}$ of 0.15 (moderate turbulence) and 0.3 (high turbulence) were investigated.

Fig. 7 depicts mean and turbulent profile data captured by the 12 Vectoflow probes during BLWT pressure tests (i.e., with the building model) at Position B (see Fig. 2b) for $\overline{\theta} = 0°$. Mean and turbulent flow statistics were computed from flow velocity data taken for a duration of 360 s. Subplots containing "blue" and "orange" markers correspond to target turbulence intensities ($I_{u,T}$) of 0.15 and 0.3, respectively. Black dashed lines represent the target power law profile models where $\overline{u}(z) =$

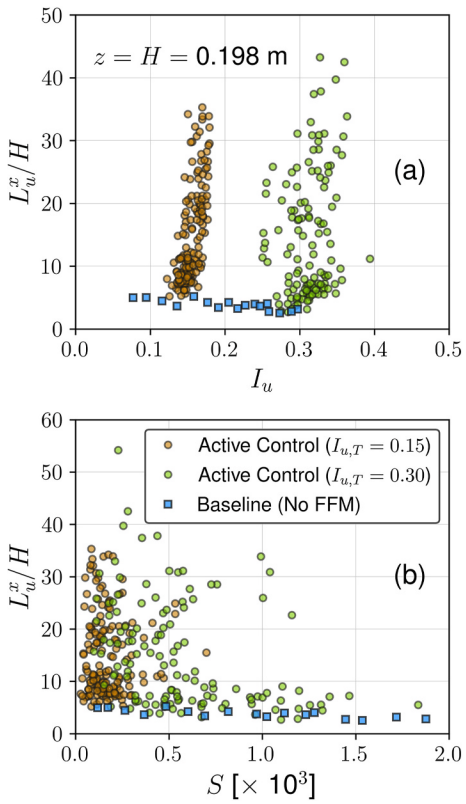

Fig. 6. Incident turbulent intensities and length scales at the BLWT test section ($x = 31.52$ m, $y = 0$ m, $z = H = 0.198$ m).

$\overline{u}_H(z/H)^{\alpha}$, $I_u(z) = I_{u,T}(H/z)^{\beta}$, $L_u^x(z) = L_{u,T}^x(z/H)^{\gamma}$, and α, β, and γ are terrain constants specified in Mokhtar et al. (2024),

Measured mean velocity profiles show very close agreement with the empirical models. Especially, target mean, and turbulence statistics closely match BLWT observations near the building height ($z = H$). As shown in Table 1, the highest target L_u^x was 7.0 m ($L_u^x/H \sim 35$) for LST-4 ($I_{u,T} = 0.15$) and LST-8 ($I_{u,T} = 0.3$). Fig. 7e and f suggests that the FFM was able to approach such length scales but was unable to reach it. Nevertheless, the FFM subsystem enable L_u^x/H values considerably larger than the ones obtained from traditional BLWT testing. While most of the turbulent scale profiles displayed a gradual increase of L_u^x/H with height, the sudden increase in L_u^x/H at the upper regions ($z/H > 5$) of LST-2 is due to a greater area under the autocorrelation curve. This is a consequence of the varying levels of LST actively generated by the different vertical cell rows of the FFM.

Injection of low-frequency fluctuations into BLWT flows can be detected in Fig. 8, which includes time series of standardized velocity fluctuations for LST tests with the lowest (LST-1 and LST-5; "teal" color) and highest (LST-4 and LST-8; "red" color) L_u^x/H estimates. The velocity signals were low-pass filtered (using a cutoff-frequency of $f_c = 5$ Hz) to reveal turbulent fluctuations at the lower frequencies. Subplots LST-4 and LST-8 display higher low-frequency fluctuations, and, at the same time, lower high-frequency turbulent energy compared to LST-1 and LST-5. This may be better illustrated in Fig. 9, which includes the corresponding (nondimensional) velocity spectra $fS_{uu}(f,H)/\overline{u}^2$ for the four velocity traces shown in Fig. 8. The black dashed curves represent the von Kármán spectral density model (Von Kármán, 1948) for isotropic turbulence defined as:

$$S_{uu}(z,f) = \frac{4L_u^x I_u^2\,\overline{u}}{f\left[1 + 70.8\left(fL_u^x/\overline{u}\right)^2\right]^{5/6}} \tag{4}$$

Albeit more pronounced in the right subplot ($I_{u,T} = 0.3$) of Fig. 9, a leftward horizontal shift in the spectral peak is noticeable for higher magnitudes of L_u^x/H. This is consistent with the spectral analysis conducted in Mokhtar et al. (2024). In the case of $I_{u,T} = 0.3$ (Fig. 9b), both LST-5 and LST-8 have very similar turbulence intensities (see Table 1), however it is evident from Fig. 9 that the distribution of the turbulent

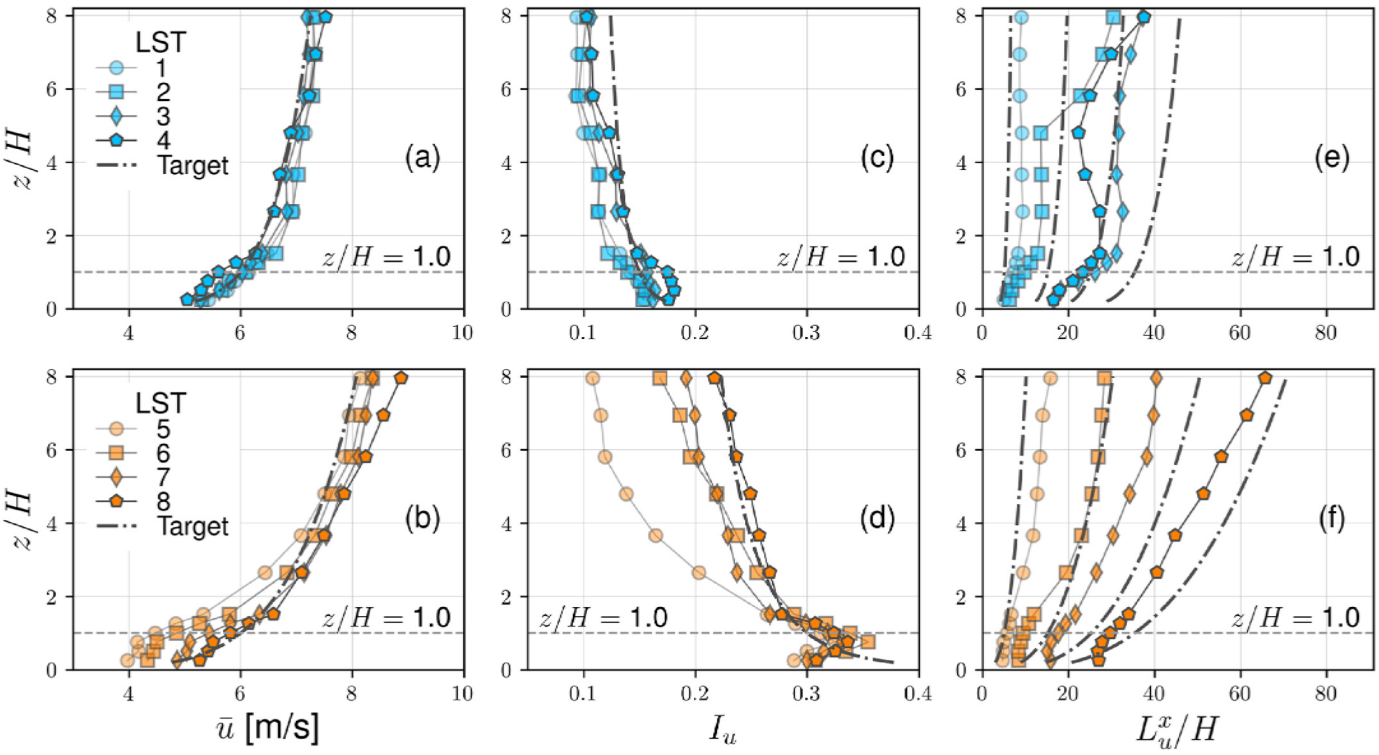

Fig. 7. Longitudinal mean (left subplots), turbulence intensity (middle subplots), and integral length scale (right subplots) profiles ($\overline{\theta} = 0°$).

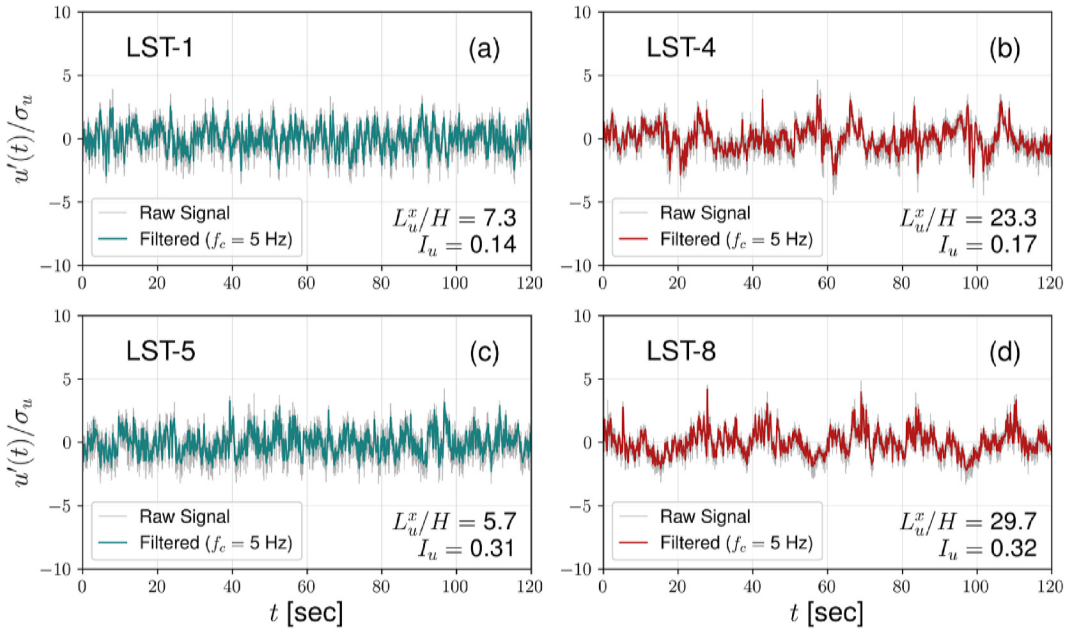

Fig. 8. Representative nondimensional velocity time histories taken at $z = 0.198$ m ($\overline{\theta} = 0°$).

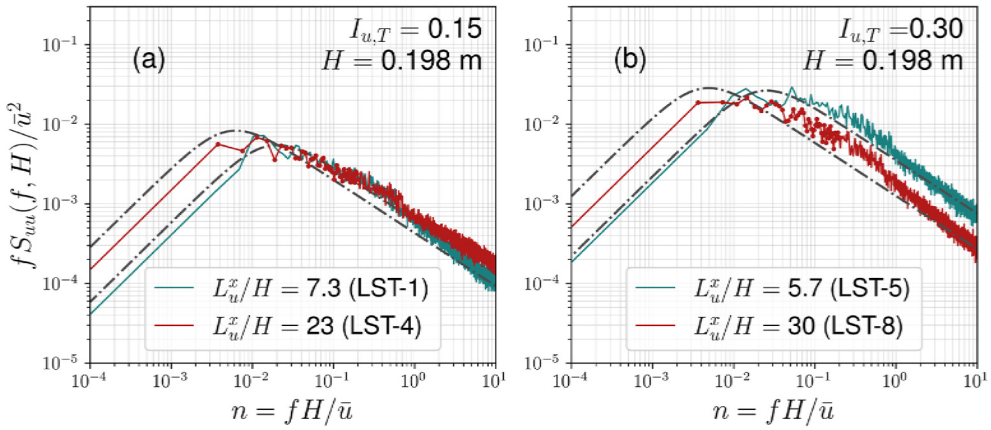

Fig. 9. Nondimensional velocity spectra at $z = H = 0.198$ m under moderate (a) and high turbulent (b) intensities.

content differs between the two LST-5 and LST-8 cases. For instance, LST-5 has higher turbulent content across the inertial subrange ($n > 0.1$), while larger levels of low-frequency turbulence ($n < 0.01$) are noticeable in LST-8. Conversely, LST cases under moderate turbulence levels ($I_{u,T} = 0.15$) displayed similar turbulent content through the inertial subrange.

3.1. Surface pressure statistics

In this work, analysis of aerodynamic roof pressure data acting on the building model was limited to wind azimuths ($\overline{\theta}$) of 0° (parallel to the longest horizontal building dimension) and 45° (cornering wind). Figs. 10 and 11 show representative mean, standard deviation (SD), and skewness pressure contours on the roof of the model for LST-5 and LST-8 ($I_{u,T} = 0.3$) under a parallel ($\overline{\theta} = 0°$) and cornering wind azimuth ($\overline{\theta} = 45°$), respectively. For $\overline{\theta} = 0°$ (Fig. 10), a clear reduction in mean pressures near the leading roof edge is evident for the larger L_u^x/H case (LST-8). At the same time, slightly larger standard deviation (SD or C_p') pressure zones are noticeable near the roof corners ('dark gray' areas) with increased turbulent scale. Interestingly, a marked rise in negative skewness values is observed under the separation 'bubble' in LST-8 compared to LST-5.

For $\overline{\theta} = 45°$, the two mean pressure contours for LST-5 and LST-8 show strong similarities in both intensity and spatial distribution, with LST-8 showing slightly larger means than LST-5 under conical vortices ('red' regions). On the other hand, SD contours shown in Fig. 11 for the higher L_u^x/H case (LST-8) display visibly stronger C_p' near the roof corner ('gray' regions) and downstream along the path of conical vortices ('white' regions). Like the $\overline{\theta} = 0°$ tests, larger skewness values of pressures were observed under for turbulent flows with greater L_u^x/H.

Fig. 12 displays local mean, standard deviation, and skewness pressure coefficients (C_p) derived from 280 s pressure time histories along roof line transects TL1 and TL2 (see Fig. 3) and $\overline{\theta} = 0°$. Like Fig. 6, 'blue' markers represent C_p obtained under moderate turbulence levels ($I_{u,T} = 0.15$), while 'orange' markers correspond to high incident turbulent conditions ($I_{u,T} = 0.3$; see Table 1). Fig. 12 suggests that for turbulence intensities around 15 % ('blue' markers), mean C_p values appear to be weakly dependent on L_u^x/H. However, a noticeable rise in $-\overline{C}_p$ near the leading roof edge ($x/H < 0.3$) is evident for LST cases tested under higher incident turbulence levels (LST 5–8; $I_{u,T} = 0.3$). This trend indicates lower $-\overline{C}_p$ with increasing L_u^x/H in the flow separation "bubble"

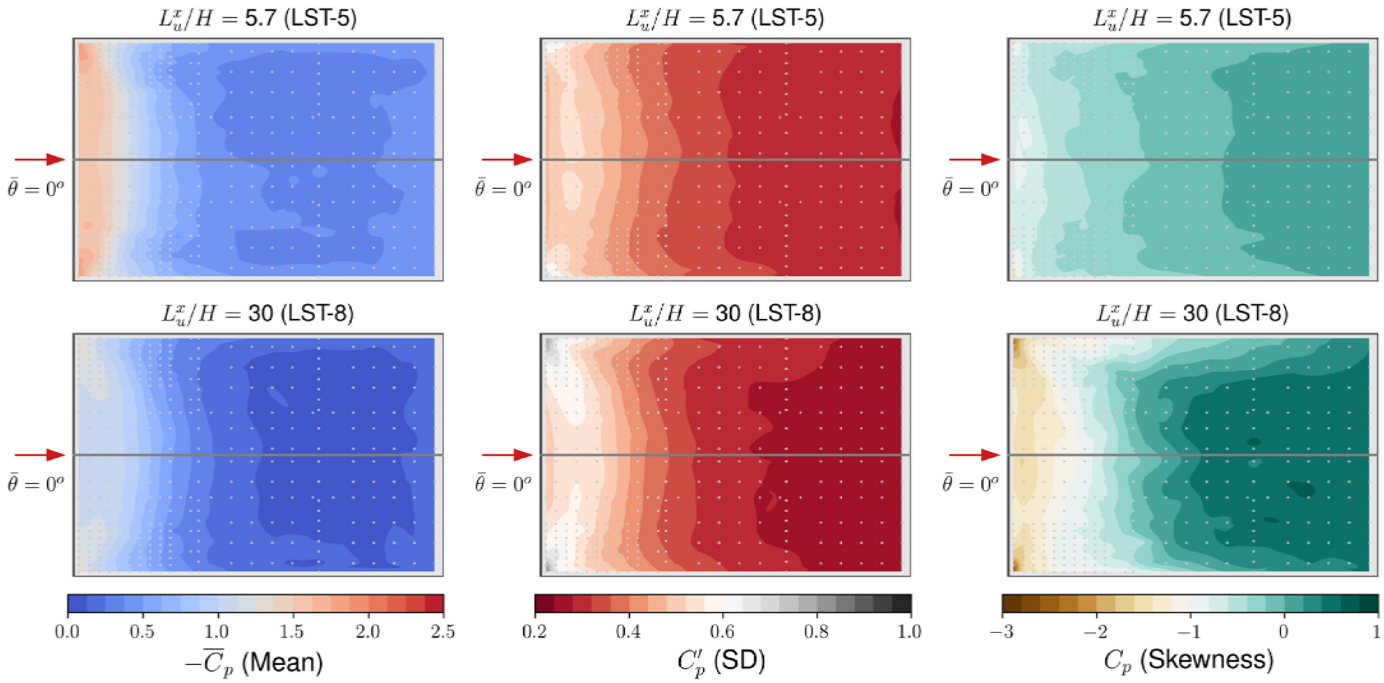

Fig. 10. Mean (left subplot), standard deviation (middle subplot), and skewness (right subplot) pressures contours ($\overline{\theta} = 0°$).

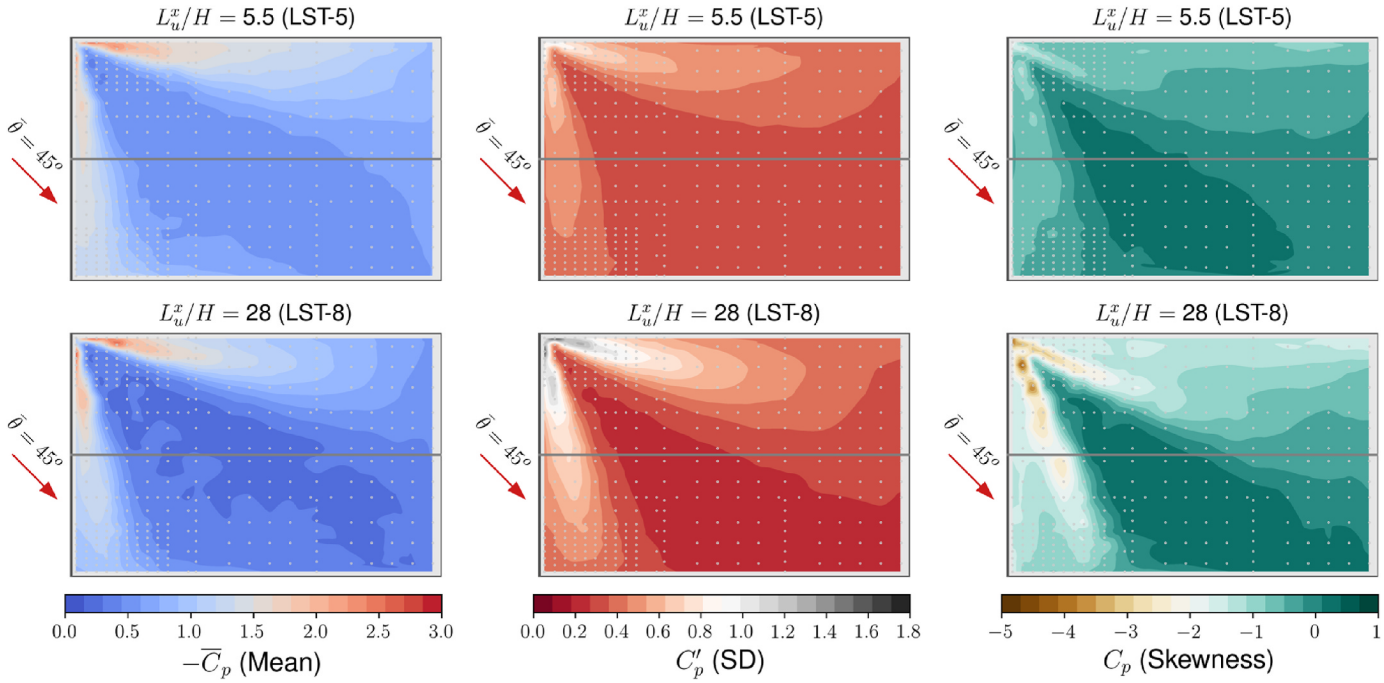

Fig. 11. Mean (left subplot), standard deviation (middle subplot), and skewness (right subplot) pressures contours ($\overline{\theta} = 45°$).

($x/H < 0.5$). For instance, at $x/H \sim 0.25$, LST-5 ($L_u^x/H = 5.7$) produced the largest magnitude of $-\overline{C}_p$, while LST-8 ($L_u^x/H = 30$) consistently showed the lowest $-\overline{C}_p$ in this roof region. This decrease in mean pressure with increasing L_u^x/H was also observed in other works of 2D wall-mounted bodies [e.g. (Li and Melbourne, 1999; Saathoff and Melbourne, 1997),].

Overall, roof line transects of standard deviation (SD) pressures (C'_p) depicted in Fig. 12 reveal a slight increase with L_u^x/H under the separation "bubble" for both turbulence levels (15% and 30%). However, both TL1 and TL2 display significantly higher magnitudes of skewness near the leading roof edge for greater L_u^x/H values. These elevated skewness values suggest an increased likelihood of higher peak pressures developed in these roof zones (investigated in Section 3.3). A detailed mapping of surface pressure statistics of corner taps for $\overline{\theta} = 45°$ can be found in Fig. 13, which includes roof line transects along TL3 (see Fig. 3) for both turbulence intensity conditions (i.e., $I_{u,T} = 0.15$ and 0.3).

3.2. Correlation of roof pressure fluctuations

The spatiotemporal correlation between local (i.e., tap) pressures

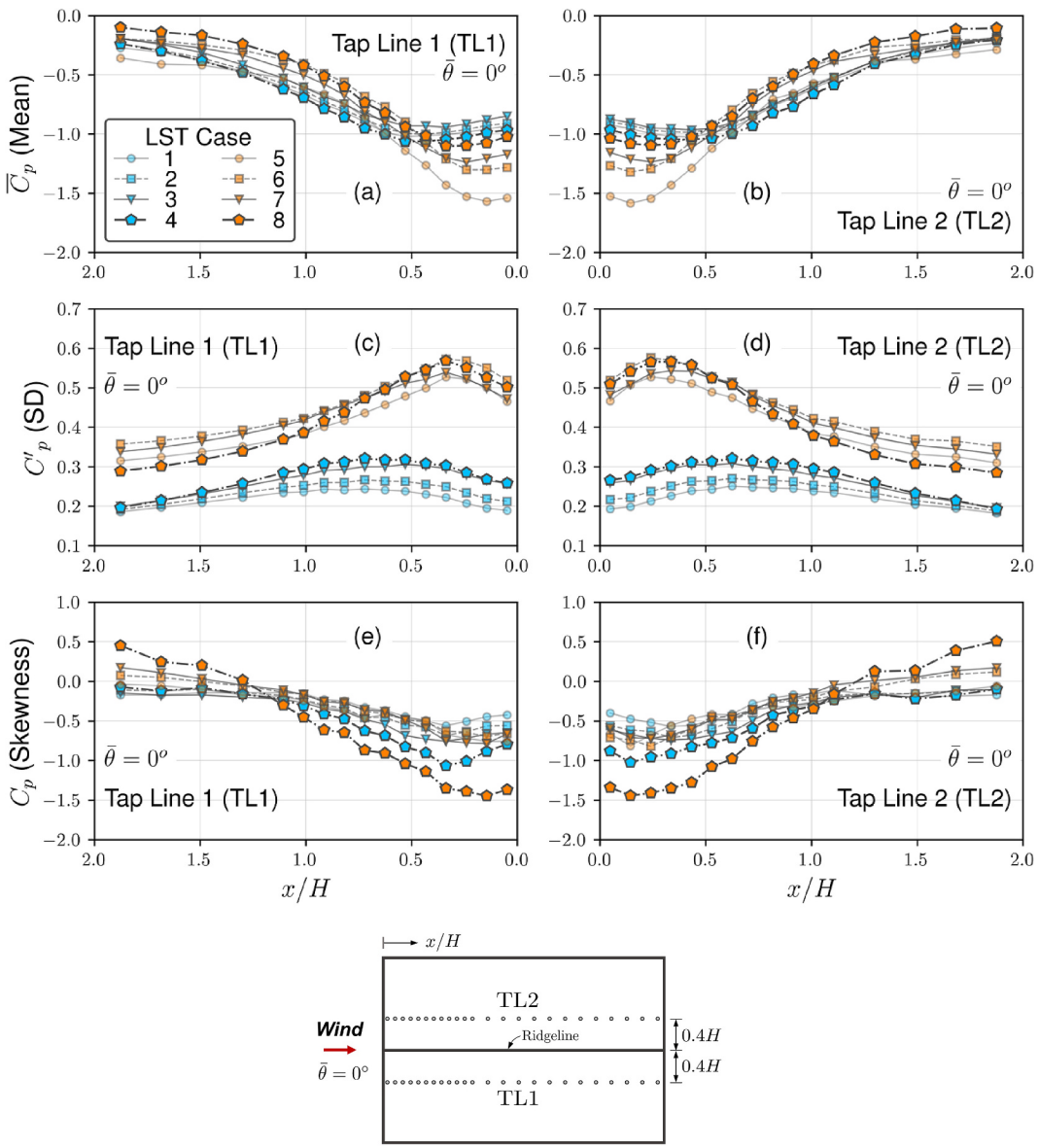

Fig. 12. Mean (a–b), standard deviation (c–d), and skewness (e–f) pressures along roof line transects TL1 (left subplots) and TL2 (right subplots) ($\bar{\theta} = 0°$).

plays a critical role in the intensity of area-average wind loads specified in codes and standards (ASCE 7-22, 2022). Some wind tunnel studies have reported greater correlation between surface pressures with increasing L_u^x/H (tested under similar turbulence intensity levels). However, these studies, including the ones of Saathoff and Melbourne (1997) and Li and Melbourne (1999), were conducted using relatively small 2D bluff-body models and tested under moderate turbulence levels (e.g., $I_u = 0.18$).

Cross-correlation of pressures along tap lines TL1, TL2, and TL3 are depicted in Fig. 14 for $\bar{\theta} = 0°$. Pearson's correlation coefficient (R_{pp}) was applied in this work, and can be defined as:

$$R_{pp} = \frac{\mathrm{cov}(p_1, p_2)}{\sigma_{p1}\sigma_{p2}} \tag{5}$$

where p_1 and p_2 are local (tap) pressure signals; $\mathrm{cov}(p_1, p_2)$ is the covariance; and σ_{p1} and σ_{p2} are the standard deviation of gauge pressure signals p_1 and p_2, respectively. For each tap line, p_1 represents the pressure signal at the first upwind tap location (e.g., Tap 1 for TL3; see Fig. 3); while p_2 correspond to the pressure signal at any other downstream tap location.

All three line transects (TL1, TL2, and TL3) in Fig. 14 reveal sharp drops in R_{pp} for LST cases corresponding to $I_{u,T} = 0.3$ and low L_u^x/H. For example, at $x/H = 0.5$, both TL1 and TL2 detected correlation values of 0.4 for LST-5 ($L_u^x/H = 5.7$), while LST-8 ($L_u^x/H = 30$) shows R_{pp} values exceeding 0.6 at the same roof location. Although not as pronounced, pressure correlations for LST cases tested under moderate incident turbulence levels ('blue' markers) also display lower R_{pp} values for smaller L_u^x/H. Interestingly, lower correlation is observed far away from the windward roof edge ($x/H\rangle$ 1.0) in LST cases with the greatest length scales. The systematic trend of increased correlation with L_u^x/H may be better visualized in Fig. 15, which offers a closeup view of R_{pp} near the roof corner ($\bar{\theta} = 45°$) for the higher incident turbulence intensity ($I_{u,T} = 0.3$).

3.3. Local peak pressure coefficients

Fig. 16 displays the cumulative distribution of minimum local peak pressures ($-\widehat{C}_p$) captured by the corner roof tap (Tap 1; see Fig. 3) for the eight LST cases and two wind azimuths ($\bar{\theta} = 0°$ and 45°). The abscissa of Fig. 16 represents the reduced variate, y_R, defined as:

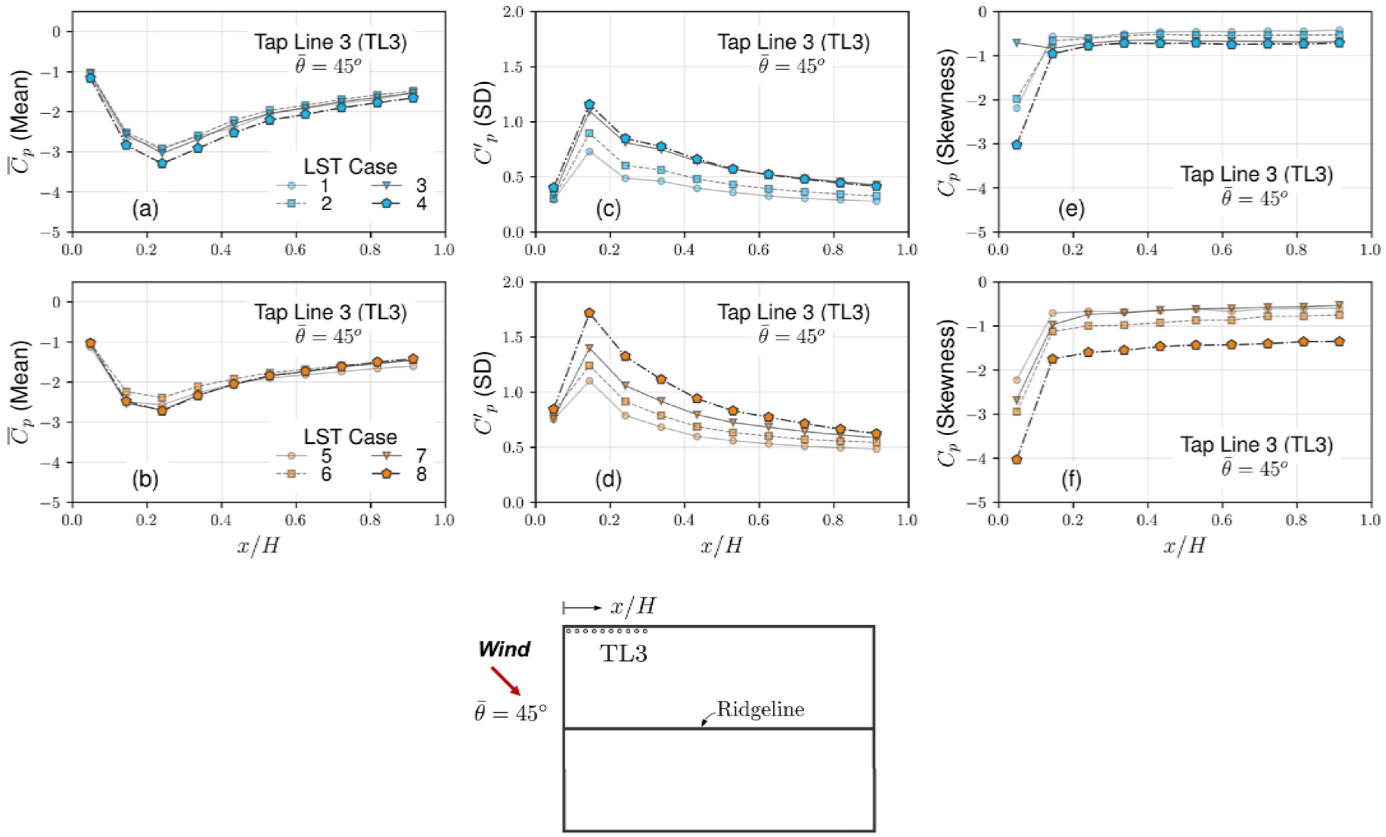

Fig. 13. Mean (a–b), standard deviation (c–d), and skewness (e–f) pressures along roof line transect TL3 ($\bar{\theta} = 45°$).

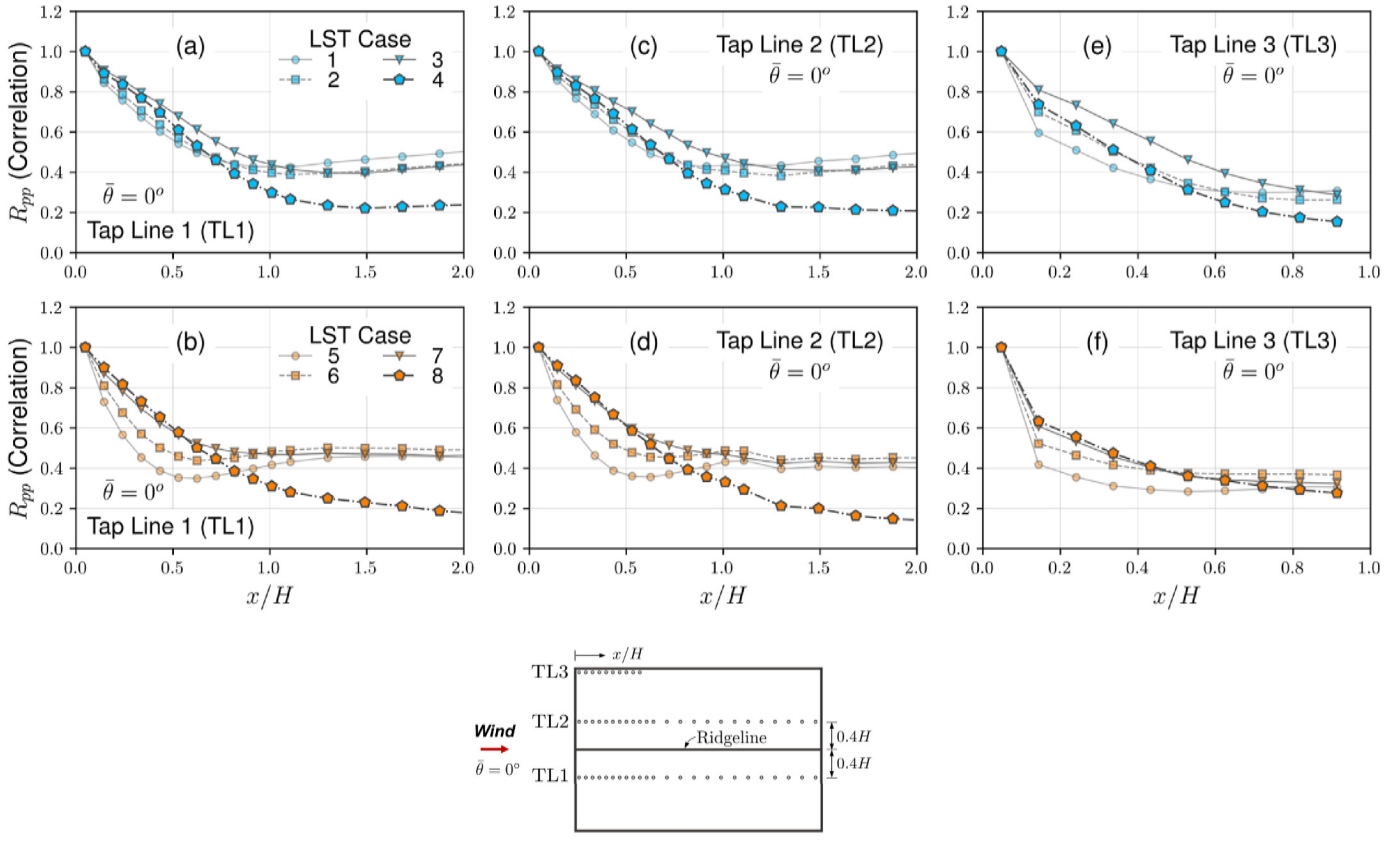

Fig. 14. Cross-correlation of pressures along roof line transects TL1 (a–b), TL2 (c–d), and TL3 (e–f) ($\bar{\theta} = 0°$).

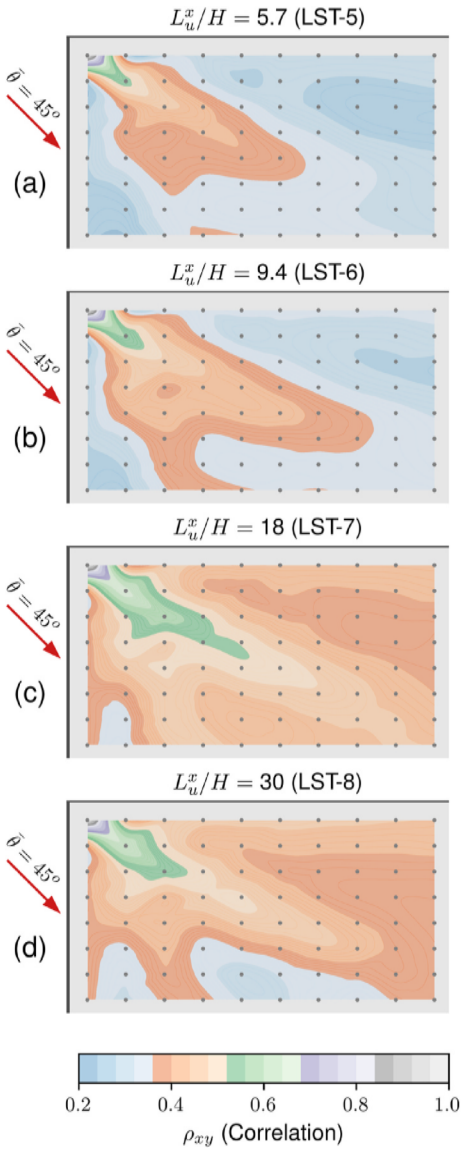

Fig. 15. Cross-correlation pressure contours near the roof corner under high incident turbulent intensities ($I_{u,T} = 0.30$).

$$y_R = -\ln\left[-\ln\left(\frac{i-0.44}{N+0.12}\right)\right] \tag{6}$$

following Gringorten (1963). In Eq. (6), N is the number of sample peaks ($N = 56$; in this work), and i is the rank order of peaks (i.e., $i = 1$ is the smallest $-\widehat{C}_p$ and $i = 56$ is the largest peak measured). Peaks were obtained by segmenting the 280 s pressure signal into 5 s non-overlapping subintervals ($N = 280/5 = 56$).

For $\overline{\theta} = 0°$ ('blue' markers), $-\widehat{C}_p$ values do not show significant differences between LST cases at Tap 1, although the largest peaks detected ($y_R \rangle 4$) occurred for the largest L_u^x/H case ('pentagonal' markers) in both $I_{u,T} = 0.15$ and 0.3. However, a greater dispersion in $-\widehat{C}_p$ is observed for the cornering wind azimuth ($\overline{\theta} = 45°$). Specifically, LST cases tested under $I_{u,T} = 0.15$ (top right subplot) systematic rise in local peaks with increasing L_u^x/H. Similar behavior is observed for $I_{u,T} = 0.3$, but the local peaks deviate from the linear relation with reduced variate values (y_R). This may be a result of the elevated turbulence intensity levels. Nevertheless, Fig. 16 suggests that the influence L_u^x/H on local peaks seems to be more pronounced for cornering horizontal wind angles. Table 2 reports the mode (M) and dispersion ($1/\alpha$) parameters from a Fisher–Tippett Type I (Gumbel) extreme value distribution for all LST cases included in Fig. 13, where $\widehat{C}_p = (1/\alpha)y_R + M$.

4. Discussion

In general, local mean and fluctuating wind pressure data monitored on flow recirculating zones display similar behavior, in terms of integral length scale effects, documented in previous wind tunnel studies performed on 2D bluff bodies (e.g. Li and Melbourne, 1999; Saathoff and Melbourne, 1997). Particularly, roof pressure data taken at $\overline{\theta} = 0°$ (wind azimuth parallel to the long building dimension) consistently demonstrated that the primary effect of LST (for the same I_u levels) is a reduction in mean pressures near the leading roof edge (under the separation "bubble"). The reduction in the magnitude of $\overline{C}_p$ with increasing L_u^x/H was more pronounced for the higher incident turbulent level investigated ($I_{u,T} = 0.30$). These observations agree with the works of Nakamura and Ozono (1987) and Li and Melbourne (1999). The former work argues that the presence LST is equivalent to slowly fluctuating upstream flows, which prevents such flows from influencing the mean pressure field on the bluff body. However, for the cornering wind azimuth ($\overline{\theta} = 45°$), a decreasing trend in mean pressure with increasing L_u^x/H was not detected in the present study. Instead, a small increase in the magnitude of $\overline{C}_p$ was seen for both the moderate ($I_{u,T} = 0.15$) and high turbulent ($I_{u,T} = 0.30$) conditions (as shown in Fig. 13). This may be a consequence of the distinctly different roof vortices that form as a consequence of oblique wind azimuths (Banks and Meroney, 2001).

Fluctuating (C_p') roof pressures along line transect parallel to the roof ridgeline ($\overline{\theta} = 0°$) showed similar trends to the ones presented in previous 2D bluff body studies (Saathoff and Melbourne, 1997; Lander et al., 2016) under moderate ($I_{u,T} = 0.15$) turbulence levels. These C_p' values displayed higher magnitudes with increasing L_u^x/H. Yet, at least for $\overline{\theta} = 0°$, negligeable differences in the magnitude and distribution of C_p' were observed under high turbulent conditions ($I_{u,T} = 0.30$) for the same line transects. The insensitivity of C_p' with increasing L_u^x/H may be due to the upstream turbulence reaching a critical condition, where the effects of turbulence on the development of the separating shear layer are saturated and would have limited alterations of the aerodynamics (Wu and Kopp, 2018, 2019). Nevertheless, this condition was only observed for line transects away from the roof corners and $\overline{\theta} = 0°$. Conversely, pressure fluctuations near roof corners generally displayed higher values with increasing L_u^x/H for $I_{u,T} = 0.30$.

Examination of higher order statistics (e.g., skewness) and cross-correlation of pressure time histories reveal stronger non-Gaussian trends and higher correlation of local (taps) pressure readings with increasing L_u^x/H; particularly in high suction zones. Observed cross-correlation of pressures indicate lower perturbation frequencies under the separated shear layer, which increases the duration of the vorticity entrainment (Saathoff and Melbourne, 1997) and allows for the development of higher peak pressures, as noted by Tieleman (2003). These observations can have implications to wind design provisions that apply area-average pressure loads (e.g., ASCE 7-22, 2022); Components and Cladding (C&C) wind loads).

Fig. 17 illustrates the influence of L_u^x/H on area-averaged peak pressures ($\widehat{C}_{p,AVG}$) near the roof corner of the building model for wind azimuths of $\overline{\theta} = 0°$ and 45° and all LST cases examined. The area-average pressure time history was computed as

$$C_{p,AVG}(t) = \frac{1}{A}\sum_{i=1}^{n_t} a_i C_{p,i}(t) \tag{7}$$

where A is the roof corner (panel) area; a_i is the tributary area of pressure tap i; $C_{p,i}(t)$ is the pressure coefficient time history of pressure tap i; and n_t is the total number of taps within the panel area A. The $\widehat{C}_{p,AVG}$

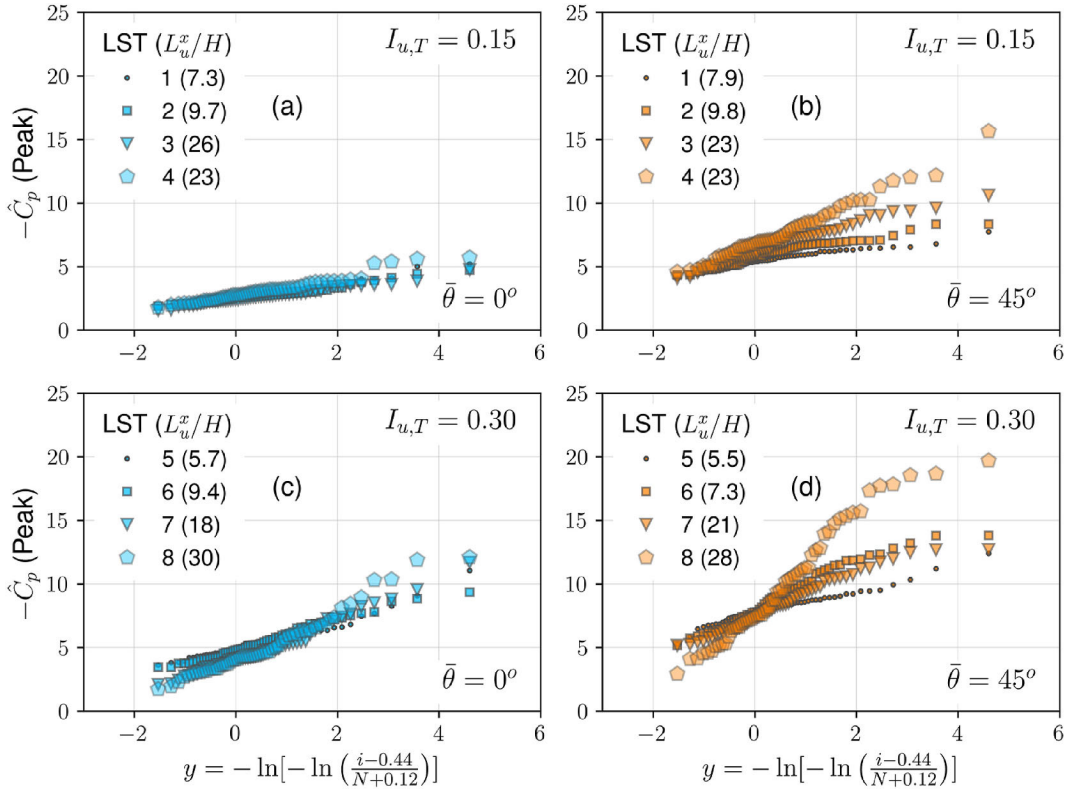

Fig. 16. Minimum (suction) pressure coefficients measured on Tap 1 ($N = 56$).

Table 2
Fitting parameters for Type I Extreme Value Distribution of $-\widehat{C}_p$ (Tap 1).

BLWT ID	$I_{u,T}$ (Target)	$L_{u,T}^x/H$ (Target)	Mode, M		Dispersion, $1/a$	
			$\bar{\theta} =$ 0°	$\bar{\theta} =$ 45°	$\bar{\theta} =$ 0°	$\bar{\theta} =$ 45°
LST-1	0.15	5.1	2.5	5.3	0.6	0.5
LST-2		15	2.5	5.6	0.5	0.8
LST-3		25	2.4	6.1	0.5	1.1
LST-4		35	2.7	6.8	0.7	1.7
LST-5	0.3	5.1	5.0	7.6	1.1	1.0
LST-6		15	4.9	8.0	1.1	1.8
LST-7		25	4.0	7.4	1.5	1.6
LST-8		35	4.1	7.9	1.8	3.4

value for the smallest panel area ($A/H^2 = 0.0062$) was calculated by averaging the local peak pressure (estimated by fitting a Fisher–Tippett Type I (Gumbel) distribution for a 78% probability of non-exceedance (Cook and Mayne, 1979) to $N = 56$ observed pressure peaks; see Fig. 16); over the four taps closest to the roof corner. On the other hand, the largest panel area ($A/H^2 = 0.30$) corresponds to the average $-\widehat{C}_p$ from 64 taps closest to the corner of the roof (i.e., all the taps within the densely tapped corner region shown in Fig. 3). The abscissa in Fig. 15 is presented in logarithmic scale to corroborate if the linear relation between $\widehat{C}_{p,AVG}$ and panel area holds for different L_u^x/H cases.

In the present work, BLWT experiments were conducted under relatively low Reynolds number values [$Re = \overline{u}H/\nu$ = (6 m/s)(0.198 m) (1.48×10^{-5} m^2/s)] compared to other BLWT tests of similar geometric scales (e.g., approximately half the $\overline{u}$ intensity reported in Fernández-Cabán and Masters (2018)). While higher *Re* conditions are generally desirable for aerodynamic building model testing, preliminary tests at the UF BLWT revealed that increasing the mean flow velocity ($\overline{u}$) influenced the FFM's effectiveness for imparting low-frequency turbulent fluctuations. For instance, a higher $\overline{u}$ (mainly driven by the vaneaxial fans) would require the FFM to generate larger low-frequency turbulent fluctuations ($\sigma_{u,Low}$ = standard deviation of low-frequency turbulence; approximately less than 5 Hz) to maintain a similar turbulence intensity level ($I_{u,Low} = \sigma_{u,Low}/\overline{u}$). As the mean velocity is increased, the discharge velocity limits of the FFM cells will be reached before the maximum $\overline{u}$ can be achieved. A more detailed discussion of this limitation is documented in Mokhtar et al. (2024). Nevertheless, statistics of pressure measurements seem to agree with past wind tunnel studies, which is likely due to the sharp-edged nature of the building specimen (i.e., rounded/curved geometries have proven to be more sensitive to *Re*).

While the scope of this work was limited to longitudinal turbulence characteristics, subsequent studies will examine the impact of the lateral (spanwise) and vertical flow velocity components and their role in the development of surface pressure fluctuations. Information derived from 3D wind velocity data (e.g., instantaneous wind azimuth and elevation angles) are readily applied in the development of quasi-steady (Q-S) models (e.g. Banks and Meroney, 2001; Richards and Hoxey, 2004; Wu and Kopp, 2016) to infer the instantaneous pressure field acting on buildings. Specifically, most Q-S models were developed to predict the effects of integral length scales significantly larger than the building dimension (e.g., eave height = *H*), which are not possible to simulate in the BLWT using traditional (i.e., passive) flow conditioning approaches.

As mentioned in Mokhtar et al. (2024), while active FFM turbulence modulation procedures were effective in generating low-frequency velocity fluctuations of the streamwise (*u*), control of the incident spanwise (*v*) and vertical (*w*) wind turbulence was not attempted. The work reported that *v* and *w* were mostly insensitive to significant increases in L_u^x/H. Nevertheless, time synchronized pressure and 3D velocity measurements will be used in future research to investigate the performance and robustness of QS models for predicting peak pressures on building structures.

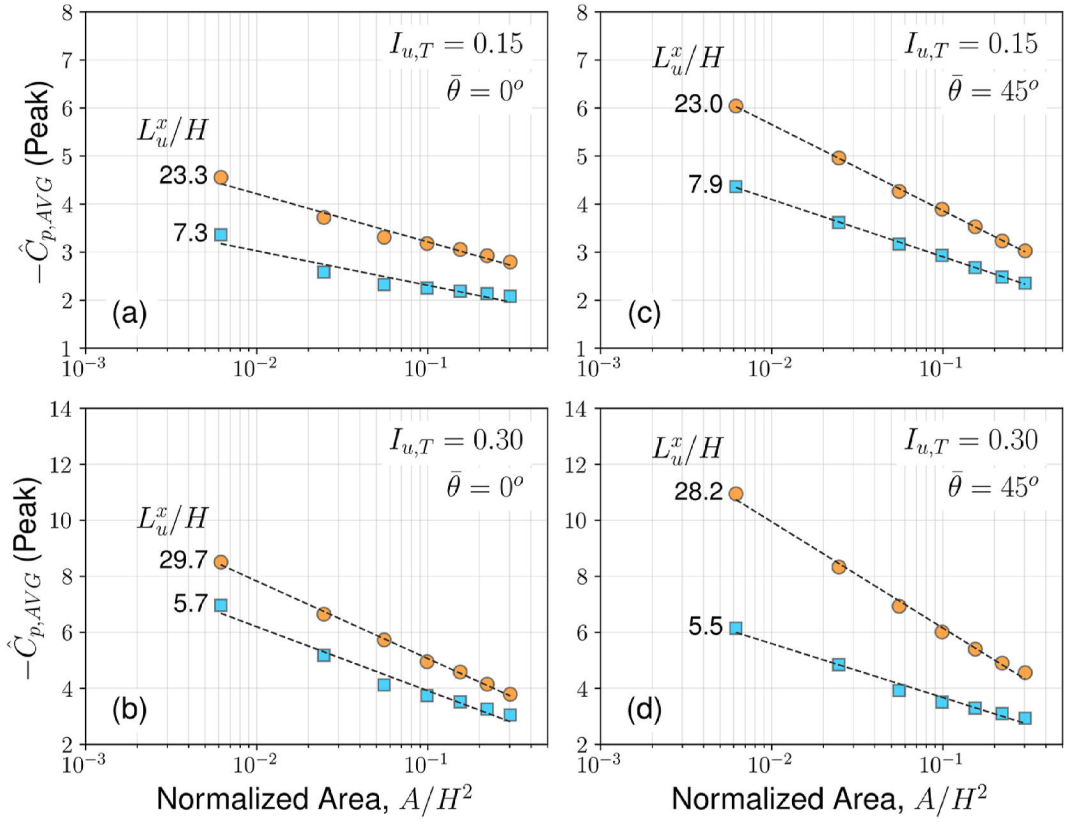

Fig. 17. Area-averaged peak pressures near the roof corner of the 1:20 TTU model for $\bar{\theta} = 0^\circ$ (a–b) and $\bar{\theta} = 45^\circ$ (c–d).

5. Conclusions

A series of aerodynamic tests were performed in a large BLWT to investigate the dependence of mean and fluctuating building pressures on the low-frequency turbulent content of incident wind fields. The research leveraged an active turbulence modulation instrument to inject low-frequency wind velocity fluctuations into BLWT flows. The instrument generated larger turbulent length scales than those produced through traditional (passive) BLWT flow conditioning approaches (e.g., spire/roughness configuration). Four L_u^x/H conditions were investigated for two turbulence intensity levels ($I_{u,T} = 0.15$ and 0.3). Simultaneous pressure measurements were monitored on the roof of a 1:20 scale low-rise building model, particularly near roof edges and corners (e.g., flow detachment zones). The following conclusion can be inferred from the statistical analysis of BLWT pressure data:

- Mean and standard deviation pressure coefficients on the roof were only slightly sensitive to L_u^x/H conditions for moderate turbulent intensity levels ($I_u = 15$ %).
- For higher turbulence intensities ($I_u = 30$%), the magnitude of negative mean pressure coefficients under the separation "bubble" was attenuated with increasing L_u^x/H for wind azimuths parallel to the longest horizontal building dimension ($\bar{\theta} = 0^\circ$).
- A significant rise in local (tap) peak pressures was detected for greater turbulent length scales, particularly for the cornering wind direction ($\bar{\theta} = 45^\circ$).
- Under similar I_u levels, larger L_u^x/H values appear to:
  - ○Intensify non-Gaussian behavior (i.e., higher skewness values of pressure signals) in high suction pressure zones. This trend was observed for all LST cases and wind azimuths considered.
  - ○Increase the spatiotemporal correlation of pressure fluctuations near roof corners and edges, leading to higher magnitudes of area-averaged wind pressures often used in wind load provision (ASCE 7-22, 2022).

Subsequent research will use this study as a baseline to examine LST effects on building envelopes with more intricate roof edge/corner geometries (e.g., parapets, spoilers, etc.). Future work will also investigate the 3D incident turbulent features and their role in developing extreme suction loads under the separation "bubble". Finally, the dataset will be used to assess and refine QS models (e.g., partial turbulence simulation) developed for large-scale wind engineering experimental facilities (Acosta et al., 2024).

CRediT authorship contribution statement

Nasreldin O. Mokhtar: Writing – original draft, Validation, Methodology, Investigation, Formal analysis, Data curation. **Pedro L. Fernández-Cabán:** Writing – review & editing, Visualization, Supervision, Project administration, Funding acquisition, Formal analysis, Data curation, Conceptualization. **Ryan A. Catarelli:** Writing – review & editing, Software, Resources, Conceptualization.

Declaration of competing interest

The authors declare that they have no known competing financial interests or personal relationships that could have appeared to influence the work reported in this paper.

Acknowledgements

This work is supported by the National Science Foundation (NSF) under CMMI Grant No. 2317176. Any opinions, findings, and conclusions or recommendations expressed in this material are those of the authors and do not necessarily reflect the views of NSF. The authors also

acknowledge the NSF NHERI EF awardees under Grant No. 2037725 and the DesignSafe-CI web-based research platform (Rathje et al., 2017) for the storage and curation of experimental data. The authors also wish to recognize the Powell Structures and Materials Laboratory staff, with special thanks to Scott Powell, Tai-An Chen, Ian Van Voris, Justin Davis, Eric Johnson, Joseph Herrera, and Rudy Wilder for their contribution to wind tunnel testing and assisting in the development of Matlab and LabVIEW code for data acquisition and analysis.

Data availability

The curated data is publicly available and can be accessed in the DesignSafe-CI Data Depot repository (Mokhtar et al., 2025).

References

Acosta, T.J., Guo, Y., Wang, J., Brusco, S., Kopp, G.A., 2024. Requirements for partial turbulence simulations using nondimensional turbulence energy contributions. J. Wind Eng. Ind. Aerod. 254, 105886.

Akon, A.F., Kopp, G.A., 2016. Mean pressure distributions and reattachment lengths for roof-separation bubbles on low-rise buildings. J. Wind Eng. Ind. Aerod. 155, 115–125.

Akon, A.F., Kopp, G.A., 2018. Turbulence structure and similarity in the separated flow above a low building in the atmospheric boundary layer. J. Wind Eng. Ind. Aerod. 182, 87–100.

ASCE 7-22, 2022. Minimum design loads and associated criteria for buildings and other structures. American Society of Civil Engineers, Reston, VA. https://doi.org/10.1061/9780784415788.

Banks, D., Meroney, R.N., 2001. The applicability of quasi-steady theory to pressure statistics beneath roof-top vortices. J. Wind Eng. Ind. Aerod. 89 (6), 569–598.

Bearman, P.W., Morel, T., 1983. Effect of free stream turbulence on the flow around bluff bodies. Prog. Aero. Sci. 20 (2–3), 97–123.

Bienkiewicz, B., Cermak, J.E., Peterka, J.A., Scanlan, R.H., 1983. Active modeling of large-scale turbulence. J. Wind Eng. Ind. Aerod. 13 (1–3), 465–475.

Cao, S., Nishi, A., Kikugawa, H., Matsuda, Y., 2002. Reproduction of wind velocity history in a multiple fan wind tunnel. J. Wind Eng. Ind. Aerod. 90 (12–15), 1719–1729.

Castro, I.P., Haque, A., 1988. The structure of a shear layer bounding a separation region. Part 2. Effects of free-stream turbulence. J. Fluid Mech. 192, 577–595.

Catarelli, R.A., Fernández-Cabán, P.L., Masters, F.J., Bridge, J.A., Gurley, K.R., Matyas, C.J., 2020a. Automated terrain generation for precise atmospheric boundary layer simulation in the wind tunnel. J. Wind Eng. Ind. Aerod. 207, 104276.

Catarelli, R.A., Fernández-Cabán, P.L., Phillips, B.M., Bridge, J.A., Masters, F.J., Gurley, K.R., Prevatt, D.O., 2020b. Automation and new capabilities in the university of Florida NHERI boundary layer wind tunnel. Frontiers in Built Environment 6, 558151.

Cook, N.J., Mayne, J.R., 1979. A novel working approach to the assessment of wind loads for equivalent static design. J. Wind Eng. Ind. Aerod. 4 (2), 149–164.

Fernández-Cabán, P.L., Masters, F.J., 2018. Effects of freestream turbulence on the pressure acting on a low-rise building roof in the separated flow region. Frontiers in Built Environment 4, 17.

Fernández-Cabán, P.L., Masters, F.J., 2020. Experiments in a large boundary layer wind tunnel: upstream terrain effects on surface pressures acting on a low-rise structure. J. Struct. Eng. 146 (8), 04720002.

Gan Chowdhury, A., Zisis, I., Irwin, P., Bitsuamlak, G., Pinelli, J.P., Hajra, B., Moravej, M., 2017. Large-scale experimentation using the 12-fan wall of wind to assess and mitigate hurricane wind and rain impacts on buildings and infrastructure systems. J. Struct. Eng. 143 (7), 04017053.

Gartshore, I.S., 1973. The effects of free stream turbulance on the drag of rectangular two-dimensional prism. University of Western Ontario, Faculty of Engineering Science, Boundary Layer Wind Tunnel Laboratory. Volumes 73-74.

Gartshore, I.S., 1984. Some effects of upstream turbulence on the unsteady lift forces imposed on prismatic two-dimensional bodies. J. Fluid Eng. 106 (4), 418–424.

Gringorten, I.I., 1963. A plotting rule for extreme probability paper. J. Geophys. Res. 68 (3), 813–814.

Guo, Y., Wu, C.H., Kopp, G.A., 2021. A method to estimate peak pressures on low-rise building models based on quasi-steady theory and partial turbulence analysis. J. Wind Eng. Ind. Aerod. 218, 104785.

Hajj, M.R., Tieleman, H.W., Tian, L., 2000. Wind tunnel simulation of time variations of turbulence and effects on pressure on surface-mounted prisms. J. Wind Eng. Ind. Aerod. 88 (2–3), 197–212.

Hillier, R., Cherry, N.J., 1981. The effects of stream turbulence on separation bubbles. J. Wind Eng. Ind. Aerod. 8 (1–2), 49–58.

Irwin, P.A., 2008. Bluff body aerodynamics in wind engineering. J. Wind Eng. Ind. Aerod. 96 (6–7), 701–712.

Jayakumari, A.K.R., Gillmeier, S., Ricci, A., Guichard, R., Blocken, B., 2023. Scaling effects on experimentally obtained pressures on an idealized building: possible implications towards asbestos containment. J. Wind Eng. Ind. Aerod. 239, 105442.

Kiya, M., Sasaki, K., 1983. Free-stream turbulence effects on a separation bubble. J. Wind Eng. Ind. Aerod. 14 (1–3), 375–386.

Kobayashi, H., Hatanaka, A., 1992. Active generation of wind gust in a two-dimensional wind tunnel. J. Wind Eng. Ind. Aerod. 42 (1–3), 959–970.

Lander, D.C., Letchford, C.W., Amitay, M., Kopp, G.A., 2016. Influence of the bluff body shear layers on the wake of a square prism in a turbulent flow. Physical Review Fluids 1 (4), 044406.

Levitan, M.L., Mehta, K.C., 1992a. Texas Tech field experiments for wind loads part 1: building and pressure measuring system. J. Wind Eng. Ind. Aerod. 43 (1–3), 1565–1576.

Levitan, M.L., Mehta, K.C., 1992b. Texas Tech field experiments for wind loads part II: meteorological instrumentation and terrain parameters. J. Wind Eng. Ind. Aerod. 43 (1–3), 1577–1588.

Li, Q.S., Melbourne, W.H., 1999. The effect of large-scale turbulence on pressure fluctuations in separated and reattaching flows. J. Wind Eng. Ind. Aerod. 83 (1–3), 159–169.

Melbourne, W.H., 1979. Turbulence effects on maximum surface pressures, a mechanism and possibility of reduction. Proc. 5th Int. Conf. On Wind Engineering. Pergamon Press, Colorado, USA, pp. 541–552.

Melbourne, W.H., 1980. Turbulence effects on maximum surface pressures-a mechanism and possibility of reduction. In: Wind Engineering. Pergamon, pp. 541–551.

Mokhtar, N.O., Fernández-Cabán, P.L., Catarelli, R.A., 2023. Generation of large-scale gust structures in a large boundary layer wind tunnel: 3D flow measurement experiments. DesignSafe-CI (Dataset). https://doi.org/10.17603/ds2-0m8r-my92.

Mokhtar, N.O., Fernández-Cabán, P.L., Catarelli, R.A., 2024. Automated large-scale and terrain-induced turbulence modulation of atmospheric surface layer flows in a large wind tunnel. Exp. Fluid 65 (1), 5.

Mooneghi, M.A., Irwin, P., Chowdhury, A.G., 2016. Partial turbulence simulation method for predicting peak wind loads on small structures and building appurtenances. J. Wind Eng. Ind. Aerod. 157, 47–62.

Mokhtar, N.O., Fernández-Cabán, P.L., Catarelli, R.A., 2025. Wind Tunnel Pressure Measurements on a 1:20 TTU-WERFL Building Model Tested under Actively Generated Large-Scale Turbulent Flows. DesignSafe-CI (Dataset). https://doi.org/10.17603/ds2-2egh-ey26.

Morrison, M.J., Kopp, G.A., 2018. Effects of turbulence intensity and scale on surface pressure fluctuations on the roof of a low-rise building in the atmospheric boundary layer. J. Wind Eng. Ind. Aerod. 183, 140–151.

Nakamura, Y., Ozono, S., 1987. The effects of turbulence on a separated and reattaching flow. J. Fluid Mech. 178, 477–490.

Nishi, A., Miyagi, H., 1995. Computer-controlled wind tunnel for wind-engineering applications. J. Wind Eng. Ind. Aerod. 54, 493–504.

Nishi, A., Miyagi, H., Higuchi, K., 1993. A computer-controlled wind tunnel. J. Wind Eng. Ind. Aerod. 46, 837–846.

Nishi, A., Kikugawa, H., Matsuda, Y., Tashiro, D., 1997. Turbulence control in multiple-fan wind tunnels. J. Wind Eng. Ind. Aerod. 67, 861–872.

Nishi, A., Kikugawa, H., Matsuda, Y., Tashiro, D., 1999. Active control of turbulence for an atmospheric boundary layer model in a wind tunnel. J. Wind Eng. Ind. Aerod. 83 (1–3), 409–419.

Ozono, S., Ikeda, H., 2018. Realization of both high-intensity and large-scale turbulence using a multi-fan wind tunnel. Exp. Fluid 59, 1–12.

Ozono, S., Nishi, A., Miyagi, H., 2006. Turbulence generated by a wind tunnel of multi-fan type in uniformly active and quasi-grid modes. J. Wind Eng. Ind. Aerod. 94 (4), 225–240.

Pinyochotiwong, 2022. Advancing the Active Flow Control of Boundary Layer Wind Tunnels. University of Florida, Dissertation.

Rathje, E.M., Dawson, C., Padgett, J.E., Pinelli, J.P., Stanzione, D., Adair, A., et al., 2017. DesignSafe: new cyberinfrastructure for natural hazards engineering. Nat. Hazards Rev. 18 (3), 06017001.

Richards, P.J., Hoxey, R.P., 2004. Quasi-steady theory and point pressures on a cubic building. J. Wind Eng. Ind. Aerod. 92 (14–15), 1173–1190.

Richards, P.J., Hoxey, R.P., 2008. Wind loads on the roof of a 6 m cube. J. Wind Eng. Ind. Aerod. 96 (6–7), 984–993.

Richards, P.J., Hoxey, R.P., 2012. Pressures on a cubic building—part 2: quasi-steady and other processes. J. Wind Eng. Ind. Aerod. 102, 87–96.

Richards, P.J., Hoxey, R.P., Connell, B.D., Lander, D.P., 2007. Wind-tunnel modelling of the Silsoe cube. J. Wind Eng. Ind. Aerod. 95 (9–11), 1384–1399.

Saathoff, P.J., Melbourne, W.H., 1997. Effects of free-stream turbulence on surface pressure fluctuations in a separation bubble. J. Fluid Mech. 337, 1–24.

Shuyang, C., Nishi, A., Hirano, K., Ozono, S., Miyagi, H., Kikugawa, H., et al., 2001. An actively controlled wind tunnel and its application to the reproduction of the atmospheric boundary layer. Boundary-Layer Meteorol. 101, 61–76.

Stenabaugh, S.E., Iida, Y., Kopp, G.A., Karava, P., 2015. Wind loads on photovoltaic arrays mounted parallel to sloped roofs on low-rise buildings. J. Wind Eng. Ind. Aerod. 139, 16–26.

Tieleman, H.W., 2003. Wind tunnel simulation of wind loading on low-rise structures: a review. J. Wind Eng. Ind. Aerod. 91 (12–15), 1627–1649.

Tieleman, H.W., Reinhold, T.A., Marshall, R.D., 1978. On the wind-tunnel simulation of the atmospheric surface layer for the study of wind loads on low-rise buildings. J. Wind Eng. Ind. Aerod. 3 (1), 21–38.

Tieleman, H.W., Surry, D., Lin, J.X., 1994. Characteristics of mean and fluctuating pressure coefficients under corner (delta wing) vortices. J. Wind Eng. Ind. Aerod. 52, 263–275.

Tieleman, H.W., Ge, Z., Hajj, M.R., Reinhold, T.A., 2003. Pressures on a surface-mounted rectangular prism under varying incident turbulence. J. Wind Eng. Ind. Aerod. 91 (9), 1095–1115.

Von Kármán, T., 1948. Progress in the statistical theory of turbulence. Proc. Natl. Acad. Sci. USA 34 (11), 530–539.

Wu, C.-H., Kopp, G.A., 2016. Estimation of wind-induced pressures on a low-rise building using quasi-steady theory. Front. Built Environ. 2. https://doi.org/10.3389/fbuil.2016.00005.

Wu, C.H., Kopp, G.A., 2018. A quasi-steady model to account for the effects of upstream turbulence characteristics on pressure fluctuations on a low-rise building. J. Wind Eng. Ind. Aerod. 179, 338–357.

Wu, C.H., Kopp, G.A., 2019. Examination of the physical assumptions of a quasi-steady vector model using the integral momentum equation. J. Wind Eng. Ind. Aerod. 187, 73–84.